Cell Reports

Article

Optimizing metastatic-cascade-dependent Rac1 targeting in breast cancer: Guidance using optical window intravital FRET imaging

Graphical abstract

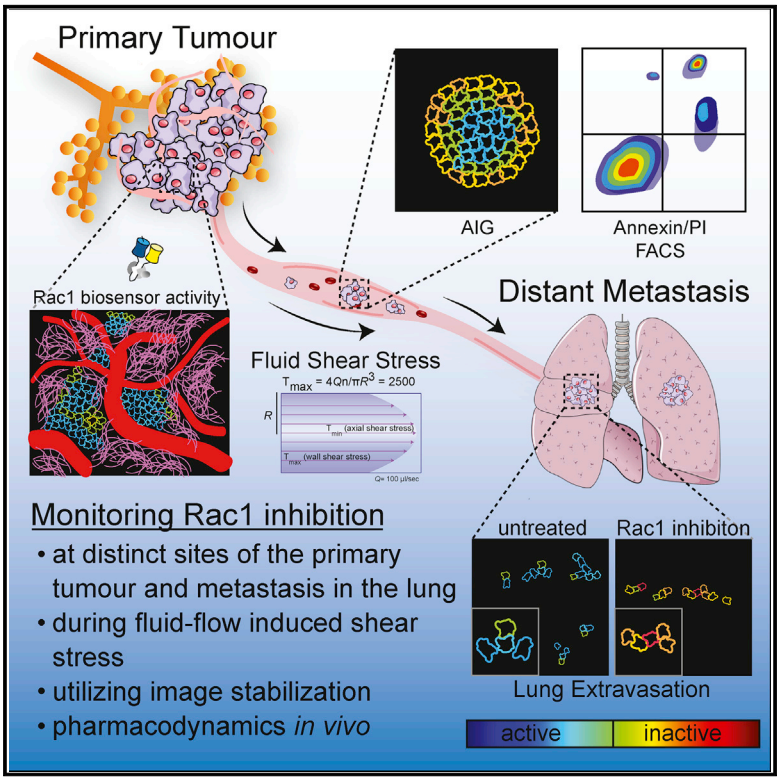

Highlights

- Invasive tumor borders and cells proximal to vessels show upregulated Rac1 activity
- Rac1 inhibition enhances tumor cell vulnerability during fluid-flow shear stress
- Live *in vivo* imaging of Rac1 activity guides optimal disease progression targeting
- Rac1 inhibition reduces intratumoral movement and lung metastasis

Authors

Alessia Floerchinger, Kendelle J. Murphy, Sharissa L. Latham, ..., Kurt I. Anderson, Paul Timpson, Max Nobis

Correspondence

p.timpson@garvan.org.au (P.T.), m.nobis@garvan.org.au (M.N.)

In brief

Floerchinger et al. use spatiotemporal imaging of a Rac1-FRET biosensor mouse to dissect the role of Rac1 in mammary carcinoma metastatic cascade. This image-guided inhibition of Rac1 scheduling at primary sites, during fluid-flow induced shear stress and dissemination vulnerabilities, results in a reduction of disease progression and lung metastasis.

Floerchinger et al., 2021, Cell Reports *36*, 109689
September 14, 2021
https://doi.org/10.1016/j.celrep.2021.109689

CellPress

Cell Reports

CellPress
OPEN ACCESS

Article

Optimizing metastatic-cascade-dependent Rac1 targeting in breast cancer: Guidance using optical window intravital FRET imaging

Alessia Floerchinger,[1,9] Kendelle J. Murphy,[1,9] Sharissa L. Latham,[1] Sean C. Warren,[1] Andrew T. McCulloch,[1] Young-Kyung Lee,[1] Janett Stoehr,[1] Pauline Mélénec,[1] Cris S. Guaman,[1] Xanthe L. Metcalf,[1] Victoria Lee,[1] Anaiis Zaratzian,[1] Andrew Da Silva,[1] Michael Tayao,[1] Sonia Rolo,[2] Monica Phimmachanh,[1] Ghazal Sultani,[1] Laura McDonald,[2] Susan M. Mason,[2] Nicola Ferrari,[2,3] Lisa M. Ooms,[4] Anna-Karin E. Johnsson,[6] Heather J. Spence,[1] Michael F. Olson,[5] Laura M. Machesky,[1] Owen J. Sansom,[2,3] Jennifer P. Morton,[2,3] Christina A. Mitchell,[4] Michael S. Samuel,[7] David R. Croucher,[1] Heidi C.E. Welch,[6] Karen Blyth,[2,3] C. Elizabeth Caldon,[1] David Herrmann,[1] Kurt I. Anderson,[2,8] Paul Timpson,[1,*] and Max Nobis[1,10,*]

[1]The Garvan Institute of Medical Research, St Vincent's Clinical School, Faculty of Medicine, UNSW Sydney, Sydney, NSW 2010, Australia
[2]Cancer Research UK Beatson Institute, Switchback Road, Bearsden, Glasgow G611BD, UK
[3]Institute of Cancer Sciences, University of Glasgow, Switchback Road, Glasgow G111QH, UK
[4]Cancer Program, Monash Biomedicine Discovery Institute, and Department of Biochemistry and Molecular Biology, Monash University, VIC 3800, Australia
[5]Department of Chemistry and Biology, Ryerson University, Toronto ON, M5B 2K3, Canada
[6]Signalling Programme, Babraham Institute, Cambridge CB223AT, UK
[7]Centre for Cancer Biology, SA Pathology and University of South Australia; and the School of Medicine, University of Adelaide, Adelaide, SA 5000, Australia
[8]Francis Crick Institute, London NW11AT, UK
[9]These authors contributed equally
[10]Lead contact
*Correspondence: p.timpson@garvan.org.au (P.T.), m.nobis@garvan.org.au (M.N.)
https://doi.org/10.1016/j.celrep.2021.109689

SUMMARY

Assessing drug response within live native tissue provides increased fidelity with regards to optimizing efficacy while minimizing off-target effects. Here, using longitudinal intravital imaging of a Rac1-Förster resonance energy transfer (FRET) biosensor mouse coupled with *in vivo* photoswitching to track intratumoral movement, we help guide treatment scheduling in a live breast cancer setting to impair metastatic progression. We uncover altered Rac1 activity at the center versus invasive border of tumors and demonstrate enhanced Rac1 activity of cells in close proximity to live tumor vasculature using optical window imaging. We further reveal that Rac1 inhibition can enhance tumor cell vulnerability to fluid-flow-induced shear stress and therefore improves overall anti-metastatic response to therapy during transit to secondary sites such as the lung. Collectively, this study demonstrates the utility of single-cell intravital imaging *in vivo* to demonstrate that Rac1 inhibition can reduce tumor progression and metastases in an autochthonous setting to improve overall survival.

INTRODUCTION

Intravital imaging is emerging as a key advance that allows us to track cellular processes within a variety of live tissues (Conway et al., 2014; Follain et al., 2020; Miller and Weissleder, 2017). Applying real-time *in vivo* imaging to assess tumor progression in its local environment has revealed time and spatial dependence of drug targeting vulnerabilities in various cancers (Conway et al., 2017; Ebrahim and Weigert, 2019; Ellenbroek and van Rheenen, 2014; Fruhwirth et al., 2011; Nobis et al., 2018; Scheele et al., 2016). To this end, we and others have employed the use of Förster resonance energy transfer (FRET) biosensor mice to explore a wide range of proteins involved in cancer progression and metastasis and their pharmacological inhibition (Festy et al., 2007; Hirata et al., 2015; Hiratsuka et al., 2015; Matsuda and Terai, 2020). For example, we have assessed fluctuations and targeting of the non-receptor tyrosine kinase Src during cancer invasion (Nobis et al., 2013), CDK1 activity in response to chemotherapy and extracellular matrix (ECM) manipulation (Vennin et al., 2017, 2019), and Akt activity in response to drug targeting in moving hypoxic regions of live tumors (Conway et al., 2018). While others have revealed stratified drug targeting and resistance to epidermal growth factor receptor (EGFR)/ERK pathway targeting in breast cancer (Komatsu et al., 2015) or altered apoptotic response to therapy *in vivo* using a caspase-3-CAAX biosensor (Janssen et al., 2013).

The small GTPase Rac1 is a key regulator of actin cytoskeletal organization and is also known to drive tumor progression and the production of reactive oxygen species (ROS) in multiple cancer types (Lindsay et al., 2011; Mack et al., 2012; Myant et al., 2013). In normal breast tissue homeostasis, Rac1 has been shown to be involved in tissue remodeling during mammary gland gestation (Akhtar et al., 2016). In a breast cancer setting, the activity of Rac1 can be co-opted and has been demonstrated to be upregulated in many cancers (Feng et al., 2014; Vega and Ridley, 2008; Yamaguchi et al., 2020). This has been partially linked to the deregulation of specific Rac1 GEFs (guanine nucleotide exchange factors) such as Tiam1 (Adams et al., 2010; Bourguignon et al., 2000a, 2000b; Li et al., 2016) or P-Rex1 (Barrio-Real et al., 2014, 2016; Liu et al., 2016; Srijakotre et al., 2020; Zhong et al., 2019) and can also be attributed to alterations of GEF/GAP (GTPase activating proteins) ratios or GDI (guanine nucleotide disassociation inhibitor) de-regulation (Hall and Nobes, 2000; Machesky and Sansom, 2012; Ridley, 2015). In some cases, this upregulation in activity can also be due to specific point mutations in Rac1 (Kawazu et al., 2013) or the upregulation of the alternative splice isoform of Rac1b (Schnelzer et al., 2000). Since Rac1 can play a key role in controlling major steps in the metastatic cascade, including coordination of cell motility, invasion, and EMT-to-MET plasticity during extravasation and colonization, it is an attractive target molecule in the treatment of cancer metastasis (Bid et al., 2013; De et al., 2019; Katz et al., 2012; Marei and Malliri, 2017). Rac1 activates the suppressor of cyclic AMP receptor mutation and WASP and verprolin homologous protein (SCAR/WAVE) complex, consequently leading to Apr2/3 actin nucleation and polymerization, which promotes lamellipodia formation and partially drives actin-based motility in 2D (Hall, 1998; Machesky and Insall, 1998). In 3D contexts, Rac1 activity has also been demonstrated to be important in the turnover of invadopodia, specific cellular structures involved in the degradation of the surrounding ECM, which often precedes tumor cell invasion and spread to secondary sites (Eddy et al., 2017; Moshfegh et al., 2014).

Using FRET imaging *in vitro*, we have previously achieved longitudinal quantification of Rac1 activity at the single-cell and subcellular level during neutrophil ROS production while also monitoring Rac1 dynamics during nascent adhesion formation in these cells prior to tracking coordinated cell migration and protrusion events during chemotaxis (Johnsson et al., 2014). Having demonstrated the potential for monitoring the volatile and rapid signaling of Rac1 GTPase *in vitro* using these highly migratory immune cells, we therefore sought to explore changes in Rac1 signaling along the steps of the metastatic cascade in a live tumor setting. In live tumors, Rac1 is also subject to oscillation to facilitate maximum tumor spread depending on the stage or site of progression (Bolado-Carrancio et al., 2020). As such, a more detailed understanding of this process is required if we are to effectively target this vital molecular switch during the multifaceted process of metastasis. Here, we aimed to look at targeting Rac1 activity in a metastatic breast cancer setting during primary growth, local invasion, dissemination in the vasculature, and subsequent colonization of metastatic sites. Using 3D organotypic modeling of tumor-ECM interactions, fluid-flow-induced shear stress assessment, and intravital imaging of Rac1 signaling in live tissue, we were able to show the benefits of inhibiting Rac1 at each step of the metastatic cascade, which could help guide fine-tuned targeting of Rac1 in breast cancer progression and spread.

RESULTS

Rac1 activity is upregulated in invasive mammary carcinoma and is spatially regulated at distinct areas within locally invasive tumors

The genetically engineered MMTV-polyoma-middle-T antigen driven mouse model of invasive and metastatic breast cancer (MMTV-PyMT), recapitulates key features of breast cancer progression and mimics locally invasive disease (Lin et al., 2003). In order to monitor Rac1 activity during disease progression, the Rac1-FRET biosensor mouse was crossed to the MMTV-PyMT-driven breast cancer model and allowed to develop invasive carcinomas for 118 ± 10 days (Figures 1A and S1A, confirming carcinoma staging via H&E; Guy et al., 1992a; Johnsson et al., 2014). Using fluorescent lifetime imaging microscopy (FLIM) to measure the lifetime of the donor fluorophore within the intramolecular and reversible Rac1-Raichu FRET reporter (Itoh et al., 2002), we could readily assess FRET and thereby Rac1 activity at the single-cell and subcellular level in complex microenvironments (Video S1). In the lifetime colormaps, inactive Rac1 (low-FRET) is represented by red/yellow colors, areas of active Rac1 (high-FRET) are represented as green/blue colors, and black depicts areas of no signal (Figures 1B and S1B). Lifetime assessments were carried out by single-cell plasma-membrane-based region of interest (ROI) selection based on the ECFP signal (Figure S1C). Age-matched wild-type (WT) mammary ducts were therefore compared to invasive carcinomas at 18 ± 3 weeks of age to reveal that Rac1 activity was highly upregulated in MMTV-PyMT-driven mammary carcinomas (average lifetime, 1.77 ± 0.04 ns; Figure 1B, green/blue in the lifetime colormap) compared to basal levels found in WT mammary glands (average lifetime, 2.20 ± 0.04 ns; Figure 1B, red/yellow in the lifetime colormap).

Having established that the overall activity of Rac1 was higher in primary carcinomas compared to normal mammary glands, we assessed whether Rac1 activity in these highly invasive carcinomas, which are known to progress to full metastases, is altered within different zones of the tumor. To achieve this, we employed mammary optical windows surgically implanted in mice with primary MMTV-PyMT tumors, allowing us to assess Rac1 activity in real time in the context of an intact vasculature and regions of local invasion (Figures 1C–1E; Video S2; Gligorijevic et al., 2009; Nobis et al., 2017; Ritsma et al., 2012, 2013, 2014). For optical windows imaging, movement artifacts induced by respiration, heartbeat, and blood flow can often interfere with FLIM-FRET imaging at the single-cell level in live tumors and act as a barrier to obtaining detailed intratumoral activity within the topology of a given tumor. To address this, we have recently developed an in-house image stabilization software package (Galene; Warren et al., 2018) for FLIM-FRET imaging to overcome this limitation (Figure 1Ci-ii; Video S3). This now allowed us to readily assess the single-cell activity of tumor cells in close proximity to live blood vasculature during flow and at sites of

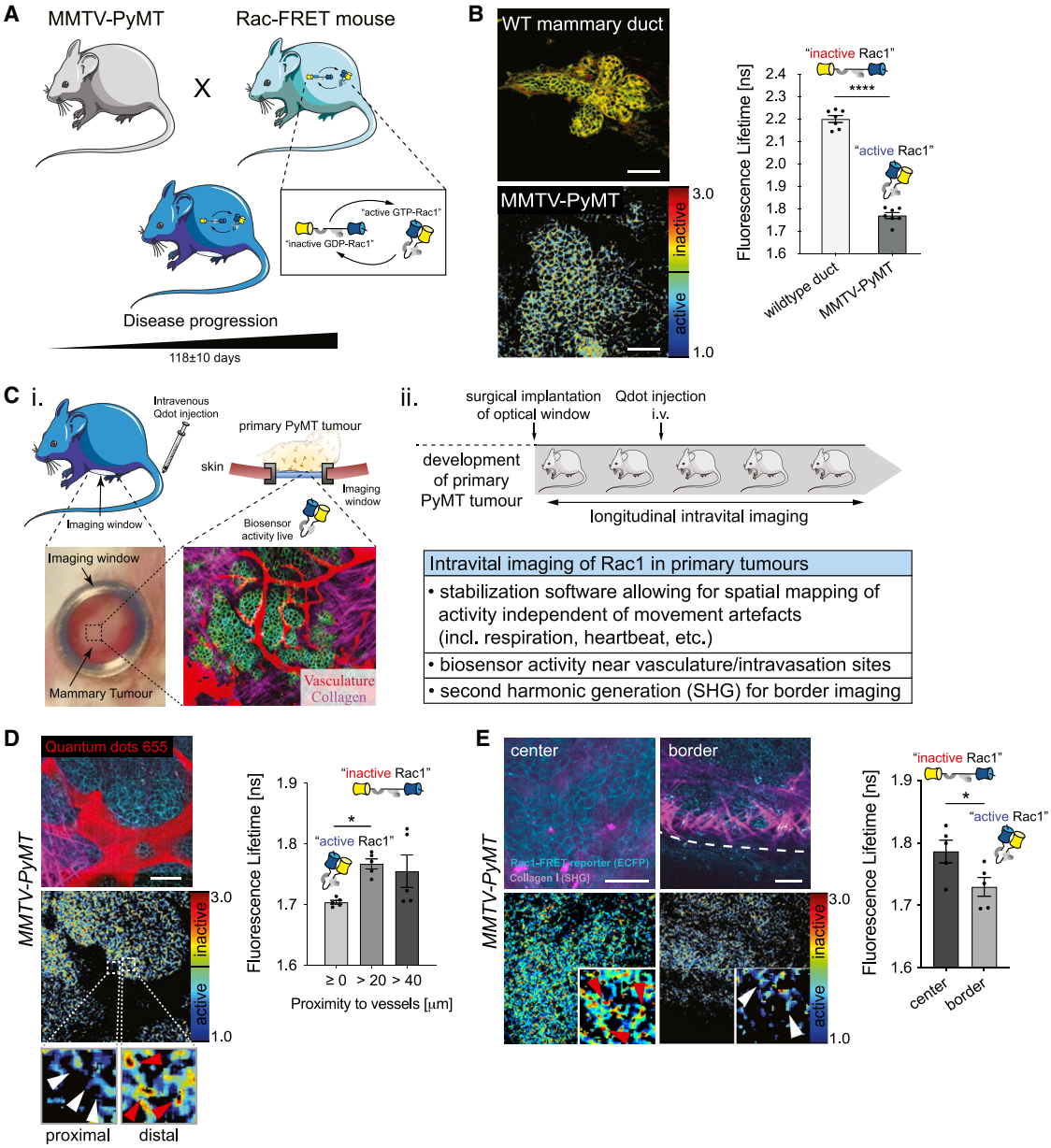

Figure 1. Rac1 signaling is increased in MMTV-PyMT-driven metastatic breast cancer

(A) Schematic of Rac1-FRET biosensor in FRET conformation upon GTP loading and Rac1 activation in cells crossed to the MMTV-PyMT-driven breast cancer model.

(B) Representative images and quantification of upregulated Rac1 activity in primary MMTV-PyMT-driven mammary tumors compared to WT mammary glands (n = 7 mice per condition, 991 cells in total).

(C) Spatiotemporal monitoring of live Rac1 activity in the context of the native tumor microenvironment showing the local vasculature (Qdot655) and second harmonic generation (SHG) imaging visualizing the local ECM monitored by optical window imaging in primary tumors (i). Longitudinal imaging can be achieved using these windows and further improved by image stabilization, allowing for the assessment of Rac1 activity in relation to tumor microenvironment (ii).

(D) Tracking of Rac1 activity in relation to the proximity of cells to local tumor vasculature, with example excerpts showing cells proximal and distal to the local vasculature (n = 5 mice, 166 cells).

(E) Upregulation of Rac1 activity at the invasive border of primary tumors as quantified through an optical window (n = 5 mice, 180 cells).

Columns show averages, and error bars represent SEM; scale bars, 50 μm. Unpaired Welch's t test, ****$p < 0.0001$ and *$p < 0.05$ (B and E); one-way ANOVA, *$p < 0.05$ (D).

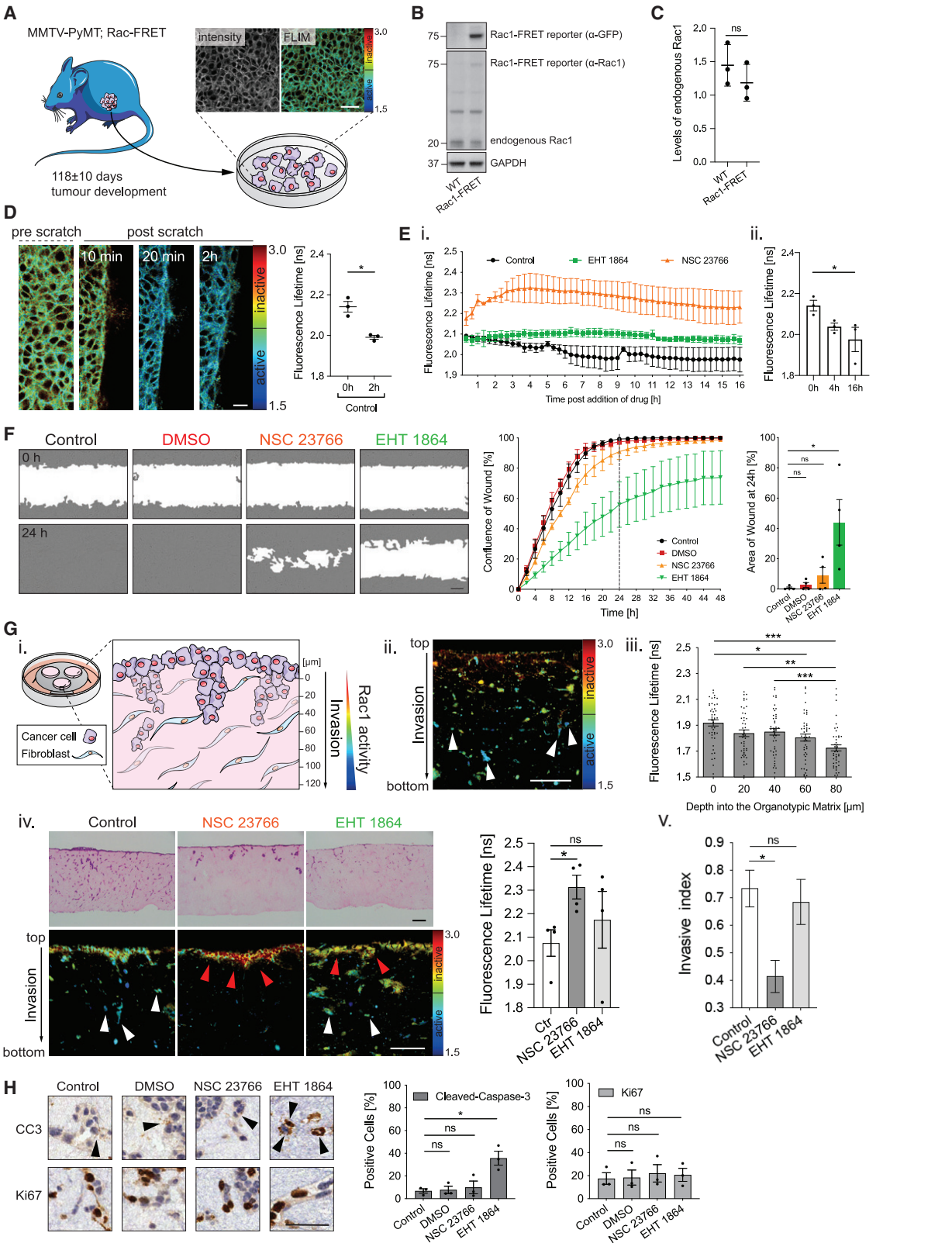

(legend on next page)

local invasion such as the tumor border versus center in locally invasive zones within carcinomas (Figures 1D and 1E).

Intravital imaging of intravenously injected Quantum dot tracker 655 as a live vascular marker (Video S2) revealed that Rac1 activity was significantly upregulated in those cells that are proximal (<20 μm) to the local vasculature and that this activity was reduced in cells further away from blood vessels within a tumor (Figure 1D; Video S2). Spatial mapping of Rac1 activity using second harmonic generation (SHG) imaging to guide assessment of tumor border versus center also revealed a significant increase in active Rac1 at the invasive border of these tumors compared to the core, in line with their highly aggressive and metastatic potential (Figure 1E, confirmed by immunohistochemistry (IHC) of phospho-PAK (S199); see Figures S1D–S1F, control WT versus heterozygous deletion of Rac1 tissue, showing a marked decrease of PAK phosphorylation; Samuel et al., 2011).

A link between upregulated Rac1 signaling in the context of ErbB2 (Her2)-driven mammary carcinoma has also been demonstrated previously via Rac1 GEF deregulation (Grasso et al., 2017; Sosa et al., 2010; Srijakotre et al., 2020). Rac1-FRET mice were therefore crossed to MMTV-Her2 mice (Guy et al., 1992b) and allowed to develop invasive carcinomas, as described above. Here, Rac1 activity was also observed to be upregulated in MMTV-Her2 tumors compared to WT mammary glands (Figure S1G), and spatial mapping via FLIM-FRET imaging revealed enhanced Rac1 activity in cells proximal versus distal to live tumor vasculature (Figure S1H). Moreover, increased Rac1 activity was evident at the tumor border compared to the core (see Figure S1I, confirmed by phospho-PAK (S199) IHC; Figures S1J and S1K). These data suggest that intratumoral spatial deregulation of Rac1 may be a general phenomenon in live tumors and led us to assess the spatiotemporal deregulation of Rac1 during motility and invasion in more detail using fluorescent primary biosensor cells generated from locally invasive carcinomas of the MMTV-PyMT; Rac1-FRET biosensor mouse.

Spatiotemporal and context-dependent inhibition of Rac1 during mammary cancer cell invasion

Next, primary cells were isolated from invasive carcinomas from MMTV-PyMT; Rac1-FRET mice, and fluorescent biosensor cell lines were established (Figure 2A, inset showing fluorescent biosensor expression at the single-cell level). Cells were analyzed for levels of endogenous Rac1 expression, and no difference was detected between cell lines expressing the Rac1-FRET biosensor and WT MMTV-PyMT cell lines isolated from tumors lacking the biosensor expression (Figures 2B and 2C). We further validated these biosensor cells as an accurate tool to assess Rac1 activity by performing overexpression experiments of known Rac1 GEFs such as Tiam1 (Malliri et al., 2002; Woodcock et al., 2009) and P-Rex1 (Liu et al., 2016) as well as Rac1 GAPs and negative regulators alpha2-Chimaerin (Beg et al., 2007) and CRYI-B (Fort et al., 2018), demonstrating expected Rac1 activation and inhibition responses respectively (Figure S2A). As Rac1 plays a key role in cytoskeletal organization and coordinated cell migration through the formation of lamellipodia at the leading edge of cells (Nobes and Hall, 1995; Ridley et al., 1992; Timpson et al., 2001), we initially performed 2D scratch assays to assess whether the primary biosensor cells respond to this spatial stimulus, as demonstrated previously in the skin and other contexts (Aoki et al., 2017; Hiratsuka et al., 2015; Kondo et al., 2021). Here, we revealed activation of Rac1 in cells at the wound edge (see Figure 2D, quantified in Figure 2Ei; Video S4), which is maintained for 16 h (Figure 2Eii), and a gradient of activation propagates from regions close to the wound edge to distal cells over time (Figures S2B and S2C). This was further validated by Rac1-GTP pull-down and phospho-PAK (S199) western blot (Figures S2D and S2E), where multiple wounds were required in order to detect these subtle and localized levels of Rac1 activation, as demonstrated previously for RhoA (Timpson et al., 2011a). FLIM-FRET imaging was then used to track Rac1 activity in tumor cells for up to 16 h during wound healing in the presence or absence of two commercially available proof-of-principle Rac1 inhibitors at previously established inhibitory concentrations: (1) NSC 23766 (50 μM), which interferes with Rac1-GEF interactions (Gao et al., 2004), and (2) EHT 1864 (20 μM) (Katz et al., 2012; Shutes et al., 2007), which binds to the active pocket of Rac1 inhibiting GTP loading (Figure 2E). Using FLIM-FRET imaging we confirmed that both Rac1 inhibitors reduced Rac1 activity and inhibited wound closure which was monitored for up to 48 h (Figure 2F), and revealed that EHT 1864 more effectively reduced 2D migration compared to NSC 23766. To test whether either Rac1 inhibitor affected proliferation or apoptosis, cells were stained for Ki67 and cleaved caspase-3 (CC3), respectively. This revealed that

Figure 2. NSC 23766 reduces Rac1 activity and inhibits invasion on 3D matrices

(A) Schematic of the isolation of a primary cell line from a MMTV-PyMT;Rac1-FRET$^{+/-}$ primary mammary tumor, scale bar, 50 μm.

(B and C) Endogenous Rac1 levels in MMTV-PyMT;Rac1-FRET cells and compared to three different MMTV-PyMT WT cell lines (B), quantified using GAPDH as a loading control (C).

(D) Rac1 is activated in a wound scratch assay, with representative images at 10-min intervals, prior to and up to 2 h after a scratch wound (n = 3; scale bar, 50 μm).

(E) Rac1 activity quantified over time after scratch wound ± Rac1 inhibitors NSC 23766 or EHT 1864 (i), showing sustained Rac1 activation up to 16 h post-scratch (ii) (n = 3).

(F) Representative images of wound closure in a scratch assay, immediately and after 24 h, quantified up to 48 h following the scratch wound (n = 4).

(G) Schematic of an organotypic matrix (i), example FLIM image of Rac1 activity in cells during invasion (ii; Rac1 active cells, white arrowheads), and quantification of Rac1 activity in relation to penetration depth of cells (iii) (n = 225 cells). Representative H&E and FLIM images of MMTV-PyMT;Rac1-FRET cells invading over a 14-day period ± Rac1 inhibitors NSC 23766 or EHT 1864 and respective quantification (Rac1 active cells, white arrowheads; Rac1 inactive cells, red arrowheads) (iv) (n = 4). Invasion index of cells treated with Rac1 inhibitors (v) (n = 4).

(H) IHC staining and quantification of organotypic matrices with cleaved caspase-3 (CC3) and Ki67 (black arrowheads) (n = 3; scale bar, 50 μm).

Columns and lines show averages, and error bars represent SEM; scale bars, 100 μm. Unpaired Welch's t test, *p < 0.05 (C, D, Eii, Giv, and Gv); one-way ANOVA, *p < 0.05, **p < 0.01, and ***p < 0.001 (F, Giii, and H).

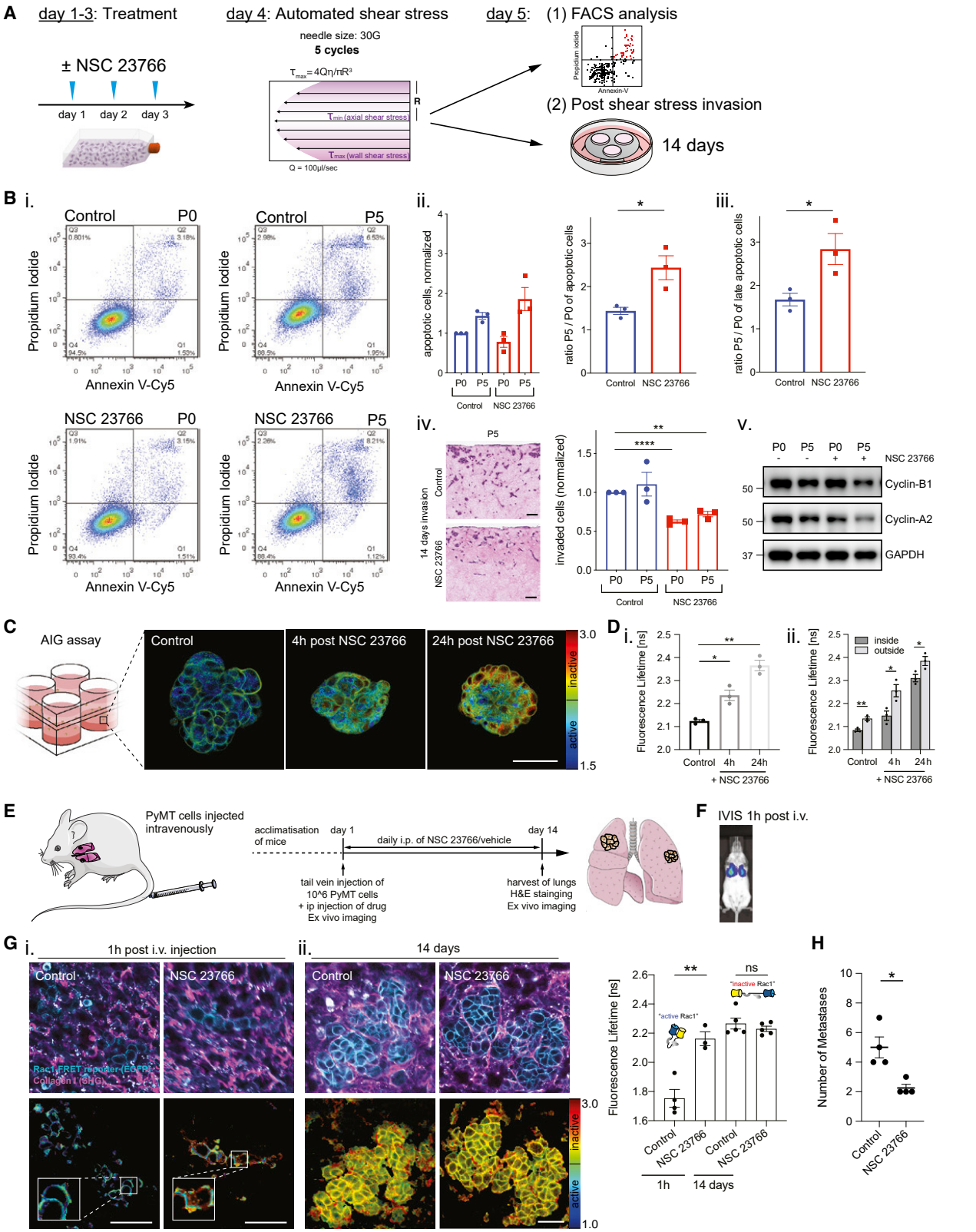

(legend on next page)

while neither compound had an effect on cell proliferation in 2D, a pronounced increase in CC3 levels was observed after treatment with EHT 1864 (Figure S2F), indicating potential off-target apoptotic effects for EHT 1864.

One of the first steps along the metastatic cascade *in vivo* involves local invasion of mammary carcinoma cells in a more complex environment and requires remodeling or break down of ECM components to facilitate invasion (Friedl and Alexander, 2011; Macpherson et al., 2014; Spence et al., 2012; Young et al., 2016). We opted to employ 3D-organotypic invasion assays in order to model this process more accurately, as previously described (Erami et al., 2016; Herrmann et al., 2014; Timpson et al., 2011b; Vennin et al., 2017, 2019). Here, cancer cells are placed upon a 3D-fibrillar collagen matrix, which had been contracted, cross-linked, and remodeled over 14 days by fibroblasts. Once formed, tumor cells are seeded on top of this matrix and can readily interact with the ECM and invade toward a chemotactic gradient (see schematic, Figures 2Gi and S2G). Using this assay, we can mimic invasive behavior in a spatially controlled environment and accurately assess Rac1 activity during this process. Multi-photon based FLIM-FRET imaging of actively invading cells within the matrix was then performed at 20 μm steps, in line with our *in vivo* assessment (Figures 1D, S1G, and S2H). This analysis revealed that cells infiltrating the matrix displayed a gradient of increased Rac1 activity concomitant with the depth of invasion (Figure 2Gii, comparing cells on top of the matrix [yellow/red in lifetime colormap] to actively invading cells [arrowheads], which appear blue in lifetime colormap, indicating full activation, quantified in Figure 2Giii). These data are in line with the local activation of Rac1 at the border of tumors *in vivo* (Figures 1E and S1I), indicating that the organotypic invasion model mimics this phenomenon in a spatially controlled 3D setting. Furthermore, to confirm these biosensor cells are an accurate tool to readout a role for Rac1 in 3D invasion in this setting, a decrease in Rac1 activity and invasion was also observed in cells overexpressing known negative Rac1 regulator CYRI-B and heterozygous knockout of the GEF P-Rex1 (Figures S3A and S3B; Fort et al., 2018; Srijakotre et al., 2020).

Next organotypic matrices were treated with Rac1 inhibitors during the process of invasion for up to 14 days, and Rac1 activity, as well as overall invasion, was quantified. Interestingly, while FLIM-FRET imaging showed that both inhibitors impaired Rac1 activity, statistically significant inhibition throughout the matrix was only observed for NSC 23766 (Figure 2Giv). Furthermore, only NSC 23766 caused a significant decrease in invasion in this 3D setting (Figure 2Gv). Specifically, in NSC 23766 treated matrices, cells remained on the surface and exhibited a robust inactivation of Rac1 and invasion (see Figure 2Giv, middle panel, red/yellow in lifetime colormap [red arrowheads]). In the EHT 1864 treated matrices, many cells maintained active Rac1 signaling and continued to invade into the matrix (see Figure 2Giv, third panel, red/yellow in lifetime colormap on top of the matrix but remaining activated/blue within the matrix during invasion [white arrowheads]). Furthermore, the decrease in invasion elicited by NSC 23766 treatment was found to be independent of changes in proliferation or apoptosis as demonstrated by Ki67 or CC3 staining (Figure 2H). However, in EHT 1864 conditions, CC3 staining again revealed a significantly elevated level of apoptosis in cells, which could potentially account for any subtle anti-invasive capacity (in line with wound-healing data; Figure S2F) and could indicate indirect toxicity for future *in vivo* assessment of this drug. We therefore focused on treatment using the inhibitor NSC 23766 as a proof-of-principle compound in subsequent experiments having demonstrated a robust 3D anti-invasive efficacy in line with the spatial activation of Rac1 we observed in invasive tumor borders *in vivo* (Figure 1E).

Rac1 inhibition enhances vulnerability to fluid-flow-induced shear stress and results in decreased dissemination and invasion of mammary cancer cells in the lung

Looking at the next key steps in the metastatic cascade, we employed fluid-flow-based shear stress to model the environmental changes cancer cells experience after traversing the endothelial layer of the vasculature (Follain et al., 2018, 2020). To mimic shear stress forces and flow, cells were subjected to automated shear stress at a flow rate of 100 μL/s with a τ_{max} = 250 Pa, which is within the range of shear stress found in physiological conditions (Figure 3A). This was repeated for five cycles, in the presence or absence of NSC 23766, as previously described (Barnes et al., 2012; Vennin et al., 2017). After exposure to shear stress, cells were assessed for alterations in early to late apoptosis by fluorescence-activated cell sorting (FACS) via Annexin V/propidium iodide staining and subjected to parallel testing of their post-shear stress invasive capacity (Figure 3A, flow chart, and Figure 3Bi). Critically, no significant difference in apoptosis was observed in cells pretreated with NSC 23766 before shear stress (P0); however, in cells that had undergone shear stress (P5), we

Figure 3. Rac1 inhibition reduces viability during shear stress conditions and reduces the establishment of lung metastasis

(A) Schematic of automated shear stress induction and subsequent FACs and post-shear stress invasion assays.

(B) Representative images of FACS analysis of MMTV-PyMT;Rac1-FRET cell viability before (P0) and after shear stress (P5) ± Rac1 inhibition with NSC 23766 (i) showing an increase in total (ii) and late apoptosis (iii). Invasion after shear stress ± Rac1 inhibition with NSC 23766 showing a decrease in invasion (iv). Response of Cyclin-B1 and Cyclin-A2 cell cycle markers before and after shear stress ± NSC 23766 (v).

(C and D) Anchorage-independent growth (AIG) assays of MMTV-PyMT;Rac1-FRET cells showing effective inhibition of Rac1 by NSC 23766 after 4 h and 24 h (C), quantified in (D) (i). AIG assessment of Rac1 activity at the outer versus inner cell layer before and after treatment with NSC 23766 (ii) (n = 3, 1,905 cells).

(E and F) Schematic of tail vein injection of MMTV-PyMT;Rac1-FRET cells ± treatment with NSC 23766 (E) and IVIS imaging after 1 h, demonstrating lung dissemination of injected cells (F).

(G) Lung imaging of MMTV-PyMT; Rac1-FRET cells showing effective inhibition of initially Rac1 activity 1 h after i.v. injection of cells (i) and overall plateaued basal Rac1 activity in established metastases after 14 days (ii) (n = 3–5 mice per group, 718 cells).

(H) Quantification of the total number of lung metastases up to 500 μm depth in 100-μm serial sections in mice ± Rac1 inhibition with NSC 23766 (n = 5 mice per condition).

Columns show averages, and error bars represent SEM; scale bars, 50 μm. Unpaired t test, *p < 0.05, **p < 0.01, and ****p < 0.0001.

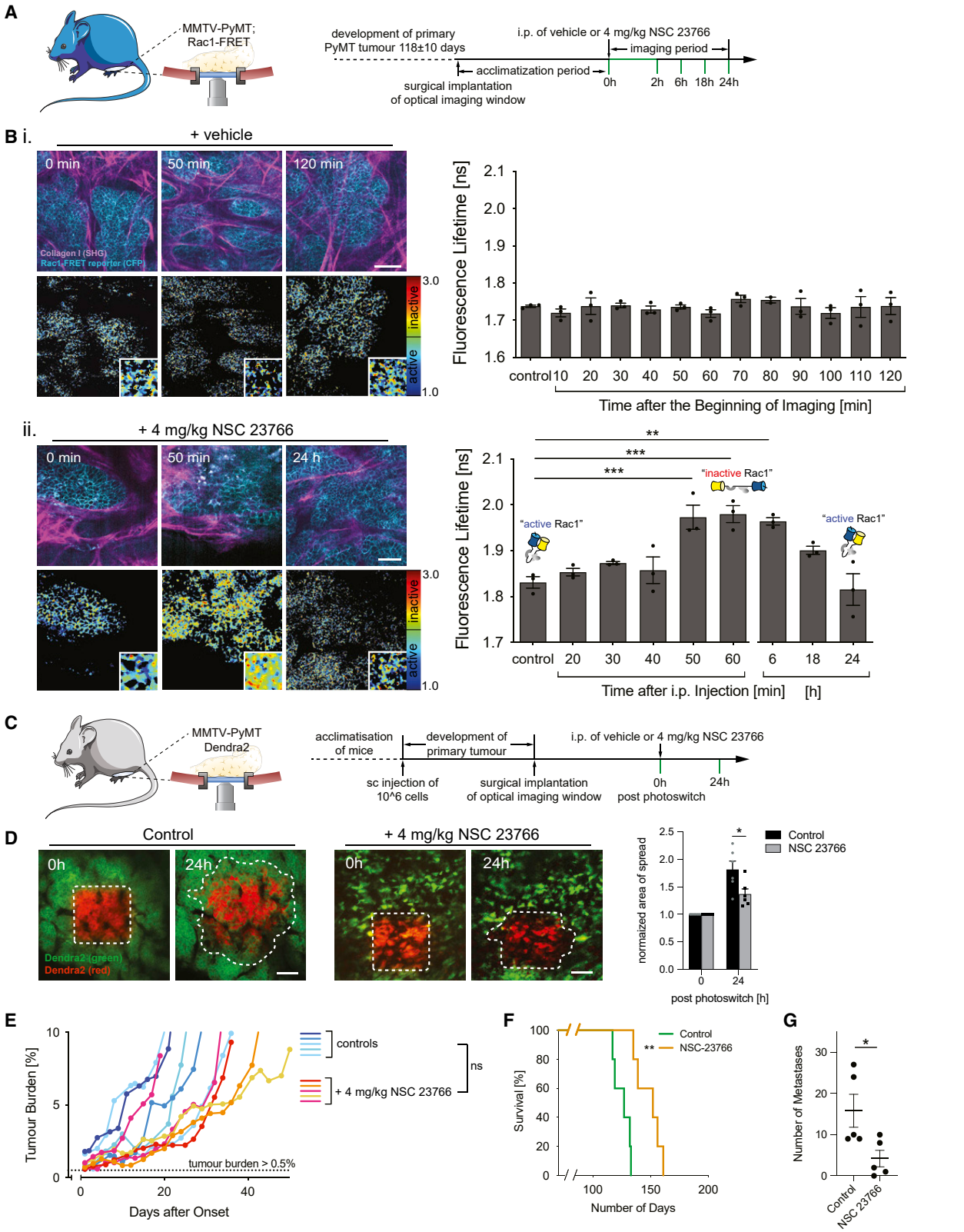

(legend on next page)

observed a significant increase in late and total apoptosis in NSC 23766 pretreated conditions (Figure 3Bii-iii). In parallel, cell invasion for 14 days post-shear stress was also examined and revealed inhibition of invasion by NSC 23766 treatment (Figure 3Biv). Coupled with the increase in apoptosis, NSC 23766 treated cells also showed decreased cyclin-A2 and B1 following shear stress, indicative of a G1 cell-cycle arrest (Figure 3Bv; Yoshida et al., 2010). Examining adhesion of MMTV-PyMT; Rac1-FRET cells to cell-derived matrices (CDMs), Rac1 was found to be effectively inhibited by treatment with NSC 23766 (Figure S3C); however, this did not result in a decrease in overall cell adhesion post-shear stress (Figure S3D). Collectively these data indicate that beyond inhibiting primary tumor invasion (Figure 2Giv-v), Rac1 inhibition may also have whole-body effects on tumor cell survival during transit in the circulation, and additionally, for those cells that do survive in the circulation, their capacity to colonize and subsequently invade into secondary tissue may be impaired. Moreover, when analyzing Rac1 activity in an anchorage-independent growth (AIG) assay to mimic cell behavior in the absence of substrate adhesion, we observed activated Rac1 in suspension which we could readily inhibit using NSC 23766 after 4 h and 24 h of treatment, respectively (see Figures 3C and 3Di, average cluster size of 75 ± 4 μm; Figure S3E; Video S5). This is in line with Rac1 and other GTPases playing an active role in AIG and cancer cell survival in transit (Follain et al., 2020; Hervieu et al., 2020; Vennin et al., 2017). Interestingly, the outer versus inner cells of AIGs were further assessed, and while cells on the periphery of clusters were inherently more inactive than cells within the center of the cluster, they were also more readily inactivated by treatment with Rac1 inhibition than cells on the inside (Figure 3Dii). This suggests that in cell clusters, a gradient of Rac1 activity may exist and cells within the center can benefit from an additional level of protection from drugs during transit.

Having explored the effects of Rac1 inhibition at several steps of dissemination, we next employed a tail vein injection model of metastatic colonization to the lung (see schematic in Figure 3E). Here, mice were treated with NSC 23766 by intraperitoneal (i.p.) injection for up to 14 days following tail vein injection of MMTV-PyMT biosensor cells. MMTV-PyMT cells could readily be detected in the lung by IVIS imaging 1 h after intravenous (i.v.) injection (Figure 3F). Moreover, single-cell FLIM-FRET imaging of the lungs at this time point allowed us to monitor Rac1 activity in cells during the early phase of extravasation and colonization and demonstrated that while Rac1 was active during this early stage of colonization (Figure 3Gi; Video S6), we could readily impair Rac1 activity in the lungs. Interestingly, Rac1 activity was also imaged 14 days post-injection to reveal that Rac1 activity had plateaued to baseline levels, impairing the capacity for further inhibition in late-stage metastases (see Figure 3Gii). Further examination of the lungs after 14 days post-colonization by H&E staining confirmed that Rac1 inhibition caused a significant decrease in the number of late-stage established lung metastases, which may partially be due to impaired survival of cells in the vasculature due to fluid-flow-induced shear stress and an impaired capacity to invade into and colonize secondary tissue post-shear stress (Figure 3H). Overall, this suggests that reduced metastatic burden observed at endpoint may be due to early-stage inactivation of Rac1 during extravasation rather than late-stage inhibition in fully formed metastases in the lung, where Rac1 levels have reduced to baseline levels, impairing the opportunity for further inhibition in late stage tumor metastases.

Rac1 inhibition reduces tumor progression, intratumoral migration, and metastases in an autochthonous setting to improve overall survival

Having established that Rac1 inhibition displays significant effects during key steps of metastatic dissemination both *in vitro* and *in vivo*, we next wanted to explore this effect in the fully developed genetically engineered mouse (GEM) model of MMTV-PyMT-driven metastatic breast cancer. To this end, MMTV-PyMT; Rac1-FRET mice were allowed to form primary mammary tumors and were engrafted with optical imaging windows (Figure 4A). This allowed for the longitudinal monitoring of drug targeting before and after treatment of a single dose of 4 mg/kg by i.p. injection. In control treatments, Rac1 baseline activity remained at steady levels over a period of 2 h (quantified in Figure 4Bi). When injected with NSC 23766, inhibition of Rac1 was evident 50 min post-injection and maintained for up to 6 h in live tumor tissue (Figure 4Bii, middle panel, from blue to yellow/red colors showing Rac1 inactivity, confirmed by orthogonal IHC staining for phospho-PAK (S199); Figures S4A and S4B). At 24 h post-injection, Rac1 activity returned to basal levels (quantified in Figure 4Bii). The longitudinal monitoring of Rac1 inhibition within live native tissue allowed us to gauge the maximal effect on Rac1 activity post treatment and guided how often the drug should be administered to be effective *in vivo*. Interestingly, *in vivo* validation of a higher dose of the Rac1 inhibitor (8 mg/kg) showed no improved efficacy toward Rac1 inhibition kinetics. Specifically, inhibition was also evident within 50–60 min of administration, and reactivation of Rac1 was similarly

Figure 4. Rac1 inhibitor NSC 23766 treatment can be monitored live *in vivo* and leads to reduced intratumoral cell motility and a reduction in lung metastasis in PyMT mice

(A) Schematic and timeline of *in vivo* pharmacodynamic monitoring of Rac1 inhibition using optical imaging windows over primary PyMT mammary tumors.

(B) Representative intensity images (top: Rac1-FRET reporter in cyan and SHG imaging in magenta) and quantification of Rac1 activity (bottom: FLIM) ± Rac1 inhibition with NSC 23766 through optical imaging windows in control mice treated with vehicle (i) and mice treated with 4 mg/kg NSC 23766 i.p. (ii) (n = 3 mice).

(C) Schematic and timeline of the establishment of Dendra2-expressing PyMT primary tumors and *in vivo* monitoring of intratumoral cell migration ± Rac1 inhibition.

(D) Representative images of Dendra2 imaging post-photoswitching and quantification of the area of spread normalized to 0 h (n = 6 versus 6 mice).

(E and F) Quantification of tumor burden MMTV-PyMT mice ± daily treatment of Rac1 inhibitor NSC 23766 (E) and overall survival (F).

(G) Quantification of lung metastasis in MMTV-PyMT mice (n = 5 mice per treatment condition).

Columns show averages, and error bars represent SEM; scale bars, 50 μm. One-way ANOVA, ****$p < 0.0001$ and ***$p < 0.001$ (B); unpaired Welch's t test, *$p < 0.05$ (D and G); and log-rank Mantel-Cox test, **$p < 0.01$ (F).

evident at 24 h, comparable to the lower-dose treatment regimen (Figure S4C, schematic; and Figure S4D, middle panel, from blue to yellow/red colors showing Rac1 inactivity).

Guided by this single-cell *in vivo* assessment, we therefore opted to use the lower dose to maximize Rac1 inhibition, while minimizing potential off-target effects. In conjunction with this, we also assessed whether this 24-h pulsed regimen of Rac1 inhibition would result in any functional readouts within this time frame, such as changes in intratumoral migration, which can often precede invasion. Primary MMTV-PyMT cells expressing the Dendra2 photoswitchable probe were allowed to form primary tumors for 53 ± 2 days in the mammary fat pad of mice and implanted with optical imaging windows (Figure 4C; Canel et al., 2010; Kedrin et al., 2008). UV-mediated photoswitching in a defined region of the tumor was then performed in the presence or absence of Rac1 inhibition, allowing us to track cell movement within live tumors over a 24-h time period (see Figure 4D, pre-photoswitched cancer cells [Dendra2-green] versus a demarcated zone of photoswitched cancer cells in red, at time 0 h and 24 h). A significant decrease in the area of photoswitched cells was observed 24 h post-photoswitch with the Rac1 inhibitor compared to controls, which was independent of effects on cell proliferation as assessed by Ki67 staining (see Figure S4E) and changes in overall cell numbers per photoswitched ROI (see Figure S4F). This indicated that the single-cell *in vivo* assessment described above resulted in a potential impairment of intratumoral migration within this short 24-h time frame concurrent with the kinetics of Rac1 inactivation within tumors (Figure 4D; Video S7).

Steered by this reduction in intratumoral migration, we assessed whether Rac1 inhibition every 24 h altered tumor onset, burden, and metastasis in long-term survival studies. Here, we found that once palpable primary tumors were identified (average size 24.9 ± 12.7 mm^3; Figure 4E; STAR Methods), i.p. injections of 4 mg/kg NSC 23766 every 24 h resulted in a significant increase in overall survival of these mice compared to control (Figure 4F). Importantly, the total number of metastases detected in the lungs of these mice was significantly decreased following pulsed Rac1 inhibition, which could partially play a role in the improved survival of these mice compared to control (Figure 4G). Collectively, these data demonstrated the potential therapeutic benefit in targeting Rac1 signaling in the context of metastatic breast cancer and demonstrates the utility of intravital-imaging-based guidance for drug targeting at distinct stages of the metastatic cascade.

DISCUSSION

The 5-year survival rate of patients with breast cancer has progressively increased over the past decades due to earlier tumor detection and improved treatment opportunities. However, once breast cancer becomes invasive and spreads to secondary sites, the 5-year survival rate drastically drops from 99% for localized tumors to 27% for distant breast cancer (Siegel et al., 2020). Consequently, the development of more effective strategies to target and treat breast cancer spread are urgently needed (Steeg, 2016). Using a proof-of-principle Rac1 inhibitor in the context of 3D organotypics, fluid-flow-based shear stress assessment, and the intravital imaging approaches outlined in this study, we demonstrate how monitoring key aspects of tumor metastasis in breast cancer can provide a more informed route to effectively target key molecules involved in distinct aspects of metastatic spread. Being able to resolve the spatiotemporal regulation of Rac1 in a continuous and holistic manner at different sites and organs opens up new avenues for us to dissect the potential global or whole-body effects of targeting Rac1 at multiple stages of disease progression and warrants fine-tuned targeting in future with standard-of-care therapy.

Rac1 activity has been shown to play an integral part in breast cancer signaling (Schnelzer et al., 2000), which was evident here by upregulation of Rac1 activity in primary lesions of MMTV-PyMT- and MMTV-Her2-driven breast cancers. We and others have recently shown that this activation is partially dependent on the activity of the Rac1 GEF P-Rex1 in both tumor models (Srijakotre et al., 2020) and breast cancer migration (Marei et al., 2016). Spatially defined Rac1 activity at the locally invasive sites of both MMTV-PyMT- and MMTV-Her2-driven tumors was particularly striking here and a similar observation of spatially defined Rac1 activity at the invasive edge in a glioblastoma model has been described previously (Hirata et al., 2012). These observations in turn may be due to the recently demonstrated involvement of the small GTPase in sensing and increasing cellular surface stiffness to enhance invasion into extracellular spaces (Kunschmann et al., 2019). Furthermore, higher Rac1 activity encountered in close proximity to local tumor vasculature may point toward cells being more poised to move when in proximity to vessels than further inside the solid tumor mass. This could also be associated with alteration of the actin cytoskeleton during the early stages of intravasation (Yamaguchi and Condeelis, 2007), which could be activated in response to either chemotactic gradient from growth factors in the local vasculature or changes in hypoxic gradients within the tumor microenvironment. In this current study, we demonstrate that Rac1 activity gradually increased as cells invade toward a chemotactic gradient (Figure 2Gii-iii). Moreover, the altered Rac1 activity found in invasive cells may be induced as a response to alterations in the hypoxic gradient previously found in these settings (Conway et al., 2018), where cells encounter increased levels of hypoxia as they invade deeper within the 3D organotypic matrix. This is in line with previous work demonstrating that hypoxia can induce Rac1 activity (Du et al., 2011; Hirota and Semenza, 2001; Wang et al., 2019) and that hypoxia can drive local sites of invasion (Hoffmann et al., 2018; Lehmann et al., 2017; Liao et al., 2007).

The utility of intravital imaging and molecular FLIM-FRET readouts such as the Rac1-FRET biosensor mouse is highlighted by potential off-target effects of previously described proof-of-principle Rac1 inhibitors that have been shown in a number of settings (Dütting et al., 2015; Hou et al., 2014; Levay et al., 2013; Mills et al., 2018). These findings were corroborated by orthogonal CC3 IHC staining in this study, showing increased apoptosis in response to EHT 1864 (Figures 2H and S2F). FLIM-FRET biosensor imaging was further highlighted to be crucial in elucidating the role of volatile small GTPase signaling in light of a recent study showing the inaccurate epitope recognition of a commonly used Rac1-GTP-specific antibody in

immunofluorescence staining (Baker et al., 2020). Based on this study, this antibody may not be appropriate to visualize and validate Rac1 activity by Rac1-GTP staining, and more robust ways to measure the rapid oscillations of Rac1 activity in live tissue, such as using the Rac1-FRET biosensor mouse described here, may help bridge this gap.

In this study we also reveal that Rac1 plays a role in protecting cells from apoptosis in response to physical forces that can be found in the circulation including fluid-flow-induced shear stress (Figure 3; Follain et al., 2018, 2020). Mechanical stressors experienced by cancer cells during dissemination can further include the initial intravasation as well as later extravasation events, during which cells have to physically deform to traverse the endothelial layer. During these processes, nuclei of the cells are drastically deformed, which can govern mechanical stress sensing and apoptosis induction (Denais et al., 2016; Lomakin et al., 2020; Venturini et al., 2020). Components of the actin cytoskeletal machinery have been shown to be involved in nuclear deformation during migration, such as Arp2/3 (Thiam et al., 2016) and Rac1 via Pak1 and tubulin (Colón-Bolea et al., 2020). Rac1 has also been linked directly to the nuclear envelope and its modulation via its GEF, Tiam1, and may therefore play a key role in regulating cell survival during these processes (Woroniuk et al., 2018). Finally, Rac1 has been shown to be involved in nuclear DNA stress responses previously (Johnson et al., 2013), and most recently, the modulation of actin has been implicated in replication stress via nuclear actin (Lamm et al., 2020). Of note, ROCK, which is a downstream target of the related GTPase RhoA, has also been partially linked to maintaining cellular architecture and shape during transit and has recently been shown to play a key role in cell survival in the circulation or during cellular compression (Boyle et al., 2020; Moose et al., 2020; Vennin et al., 2017). Importantly, short-term transient priming of ROCK rather than chronic treatment was shown to be beneficial in reducing pancreatic cancer progression and spread, illustrating that fine-tuned stage-specific treatment and optimized timing of therapy during metastatic disease can result in improved outcomes while minimizing potentially unwanted off-target effects in live tumor settings.

Quantification of cellular spread inside live primary tumors using the photoswitchable probe Dendra2 in conjunction with optical windows demonstrated partial inhibition of intratumoral migration of MMTV-PyMT breast cancer cells following our optimized treatment regimen with Rac1 inhibition *in vivo*. As this represents an orthotopic injection model, there may also be other factors at play influencing baseline Rac1 activity, such as apoptosis by primary tumor cell turnover and proliferation. A difference in cell proliferation by Ki67 staining and cell number assessment of the photoswitched regions between the control and treatment cohort, however, was not observed, further indicating a stalling in intratumoral movement post-Rac1 inhibition. Furthermore, single-cell assessment of Rac1 in native mammary tissue allowed us to assess the pharmacodynamics and pharmacokinetics of Rac1 inhibition in the fully developed primary tumor of the GEM model to maximize drug dosing regimens, while minimizing potential off-target effects of unnecessarily higher drug dosing levels and administration schedules. The utility of longitudinal imaging in this way could therefore facilitate lower doses of anti-metastatic drugs to be administered in combination with standard-of-care therapy in the future, thereby improving the effectiveness of multiple drug combination approaches. Of particular interest are non-steroidal anti-inflammatory drugs (NSAIDs) currently in clinical use to treat metastatic ovarian cancer that have been demonstrated to inhibit Rac1 activity (Guo et al., 2015a; Oprea et al., 2015) and prolong survival in patients (Guo et al., 2015b; (Forget et al., 2014)). Specifically, the R-enantiomer of ketorolac has been demonstrated to inhibit Rac1 GTP loading and is indicated in suppressing early breast cancer relapse (Desmedt et al., 2018; Retsky et al., 2012).

Aberrant activity of GEF/GAP or GDIs is associated with Rac1 deregulation in breast cancers (Cherfils and Zeghouf, 2013; Marei and Malliri, 2017; Srijakotre et al., 2020), and active Rac1-GTP has been shown to be linked to shorter disease-free survival in patients with breast cancer receiving endocrine or chemotherapy (Yamaguchi et al., 2020). Specifically, P-Rex1 knockout in two models of mammary cancer has been demonstrated to slow cancer progression and reduce Rac1 activity in a dose-dependent manner measured by FLIM-FRET in WT, heterozygous, and homozygous knockout animals (Srijakotre et al., 2020). The approaches used in this study could therefore be readily performed in other specific genetic backgrounds which mimic these amplifications, mutations, or altered expression and activation profiles. In doing so, this form of stage-specific assessment could be used to inform whether (i) Rac1 activity is differentially activated at key stages of the metastatic cascade depending on the aberration modeled, and (ii) this information could be utilized to inform when best to treat and intervene in the respective genetic backgrounds in the future. Similarly, repurposing the assessment of Rac1 activity outlined in this study could be used to assess how other proto-typical Rho-GTPases such as RhoA and Cdc42 (Hodgson et al., 2016; Nobis et al., 2017, 2020), which are also known to be hijacked in cancer, can best be targeted in this disease. It has also been demonstrated previously (Byrne et al., 2016; Lawson and Burridge, 2014; Machacek et al., 2009; Ridley, 2015; Ridley and Hall, 1992; Spiering and Hodgson, 2011) that Rho and Rac activation, depending on the cell-type-specific context, may have antagonistic effects but in other contexts often also occur sequentially to promote coordinated protrusions of cells. This phenomenon could be further investigated in the future in a full tumor setting, for example, by the use of multiplexed FRET imaging (Roebroek et al., 2021) and employing optogenetic near-infrared fluorophores to simultaneously image several small GTPases (Shcherbakova et al., 2018). Furthermore, while a number of clinically relevant ROCK inhibitors are currently under assessment (clinical phase 2 trial KD025; Flynn et al., 2016), our *in vivo* model described here could also be used as a platform to assess new Rac1 inhibitor pipelines in development (Cardama et al., 2014; Marei and Malliri, 2017; Montalvo-Ortiz et al., 2012).

Finally, a number of other ancillary mechanisms have been demonstrated to be co-opted in cancer to drive disease progression and metastasis. Fortunately, a large portfolio of reversible FRET biosensors have been developed to assess aberrations in many of these pathways (Newman et al., 2011; Vennin et al., 2016) and as such can also be examined at the

single-cell to subcellular level in live tumor tissue to optimize pharmacokinetics and pharmacodynamics *in situ*. This should provide a more accurate assessment of when best to target these interconnected networks or hallmarks of cancer in a live complex tumor niche, thereby more accurately recapitulating tumor response in the context of its surrounding tissue for maximal effect.

STAR★METHODS

Detailed methods are provided in the online version of this paper and include the following:

- KEY RESOURCES TABLE
- RESOURCE AVAILABILITY
  - Lead contact
  - Materials availability
  - Data and code availability
- EXPERIMENTAL MODEL AND SUBJECT DETAILS
  - Animal models
  - Cell culture
- METHOD DETAILS
  - Plasmid constructs
  - Transient transfections and stable cell line establishment
  - 2D Scratch Assay
  - Organotypic Invasion
  - Shear Stress and FACS analysis
  - Cellular derived matrix (CDM) attachment assay
  - Anchorage Independent Growth (AIG) Assay
  - Immunohistochemistry
  - Western Blotting and Rac1 Pulldown
  - Mammary imaging window
  - *In vivo* and *Ex vivo* Imaging, Single Cell FLIM analysis and Motion Correction
- QUANTIFICATION AND STATISTICAL ANALYSIS

SUPPLEMENTAL INFORMATION

Supplemental information can be found online at https://doi.org/10.1016/j.celrep.2021.109689.

ACKNOWLEDGMENTS

The authors would like to thank the staff at the Australian BioResource, Biological testing facility, tissue culture facility under G. Lehrbach and R. Lyons, the GWCCG Core facility Flow Cytometry under E. Lam and the histology core facility under the leadership of A. Zaratzian at the Garvan Institute of Medical Research. The authors would further like to thank the staff at the Biological Services Unit, Beatson Advanced Imaging Resource and histology facility under the leadership of Colin Nixon at the CRUK Beatson Institute. The FVB/NJ 8th generation clean PyMT-20065 cell line was made available through SEARCHBreast (https://searchbreast.org/). Some images were adapted from Servier Medical Art, licensed under the Creative Commons Attribution 3.0. Unported license (http://creativecommons.org/licenses/by/3.0/). This work was supported by a Cancer Institute New South Wales (CINSW) Early Career fellowship (M.N. and D.H.), an NHMRC Ideas grant (M.N.), NBCF grants (P.T., IIRS-21-077; D.H., IN-17-070 and IIRS-18-129), an NHMRC project grant and Senior Research Fellowship (SRF) (P.T.), St Vincent's Clinical Foundation grants (M.N., D.H., P.T., and C.E.C.), an Australian Cancer Research Fund (ACRF) grant, and Suttons Family and Len Ainsworth Foundation philanthropy and Cancer Research UK core funding at the CRUK Beatson Institute (A17196).

AUTHOR CONTRIBUTIONS

Conceptualization, A.F., K.J.M., K.I.A., P.T., and M.N.; methodology, S.C.W., K.I.A, P.T., and M.N. investigation, A.F., K.J.M., S.L.L., A.T.M., Y-.K.L., J.S., P.M., C.S.G., X.M., V.L., A.Z., A.D.S., M.T., S.R., M.S., G.S., L.M., S.M.M., N.F., and M.N.; formal analysis, A.F., K.J.M., S.L.L., Y-.K.L., A.T.M., and M.N.; resources, S.C.W., L.M.O., A.-K.E.J., H.J.S., M.F.O., L.M.M., O.J.S, J.P.M., C.A.M., M.S.S., D.R.C., H.C.E.W., K.B., and C.E.C.; funding acquisition, D.H., K.I.A., P.T., and M.N.; writing – original draft, P.T. and M.N.; writing – review and editing, D.H., P.T., and M.N.; supervision, K.I.A., P.T., and M.N.; all authors critically revised the manuscript.

DECLARATION OF INTERESTS

P.T. receives reagents from Kadmon, INXMED (consultant), CRUK Astra Zeneca Alliance laboratory, RedX Pharma, Equlibre Biopharmaceuticals, and Amplia Therapeutics. Under a licensing agreement between Amplia Therapeutics and the Garvan Institute of Medical Research, K.M., D.H., and P.T. (consultant) are entitled to milestone payments. The Owen Sansom laboratory receives funding from Cancer Research Technology, Redex, Astra Zeneca, and Novartis. The remaining authors declare no competing interests.

Received: October 9, 2020
Revised: July 6, 2021
Accepted: August 18, 2021
Published: September 14, 2021

REFERENCES

Adams, H.C., 3rd, Chen, R., Liu, Z., and Whitehead, I.P. (2010). Regulation of breast cancer cell motility by T-cell lymphoma invasion and metastasis-inducing protein. Breast Cancer Res. *12*, R69.

Akhtar, N., Li, W., Mironov, A., and Streuli, C.H. (2016). Rac1 Controls Both the Secretory Function of the Mammary Gland and Its Remodeling for Successive Gestations. Dev. Cell *38*, 522–535.

Aoki, K., Kondo, Y., Naoki, H., Hiratsuka, T., Itoh, R.E., and Matsuda, M. (2017). Propagating Wave of ERK Activation Orients Collective Cell Migration. Dev. Cell *43*, 305–317.e5.

Baker, M.J., Cooke, M., Kreider-Letterman, G., Garcia-Mata, R., Janmey, P.A., and Kazanietz, M.G. (2020). Evaluation of active Rac1 levels in cancer cells: A case of misleading conclusions from immunofluorescence analysis. J. Biol. Chem. *295*, 13698–13710.

Bankhead, P., Loughrey, M.B., Fernández, J.A., Dombrowski, Y., McArt, D.G., Dunne, P.D., McQuaid, S., Gray, R.T., Murray, L.J., Coleman, H.G., et al. (2017). QuPath: Open source software for digital pathology image analysis. Sci. Rep. *7*, 16878.

Barnes, J.M., Nauseef, J.T., and Henry, M.D. (2012). Resistance to fluid shear stress is a conserved biophysical property of malignant cells. PLoS ONE *7*, e50973.

Barrio-Real, L., Benedetti, L.G., Engel, N., Tu, Y., Cho, S., Sukumar, S., and Kazanietz, M.G. (2014). Subtype-specific overexpression of the Rac-GEF P-REX1 in breast cancer is associated with promoter hypomethylation. Breast Cancer Res. *16*, 441.

Barrio-Real, L., Wertheimer, E., Garg, R., Abba, M.C., and Kazanietz, M.G. (2016). Characterization of a P-Rex1 gene signature in breast cancer cells. Oncotarget *7*, 51335–51348.

Beg, A.A., Sommer, J.E., Martin, J.H., and Scheiffele, P. (2007). α2-Chimaerin is an essential EphA4 effector in the assembly of neuronal locomotor circuits. Neuron *55*, 768–778.

Bid, H.K., Roberts, R.D., Manchanda, P.K., and Houghton, P.J. (2013). RAC1: an emerging therapeutic option for targeting cancer angiogenesis and metastasis. Mol. Cancer Ther. *12*, 1925–1934.

Bolado-Carrancio, A., Rukhlenko, O.S., Nikonova, E., Tsyganov, M.A., Wheeler, A., Garcia-Munoz, A., Kolch, W., von Kriegsheim, A., and Kholodenko, B.N. (2020). Periodic propagating waves coordinate RhoGTPase network dynamics at the leading and trailing edges during cell migration. eLife *9*, 1–34.

Bourguignon, L.Y.W., Zhu, H., Shao, L., and Chen, Y.W. (2000a). CD44 interaction with tiam1 promotes Rac1 signaling and hyaluronic acid-mediated breast tumor cell migration. J. Biol. Chem. *275*, 1829–1838.

Bourguignon, L.Y.W., Zhu, H., Shao, L., and Chen, Y.W. (2000b). Ankyrin-Tiam1 interaction promotes Rac1 signaling and metastatic breast tumor cell invasion and migration. J. Cell Biol. *150*, 177–191.

Boyle, S.T., Kular, J., Nobis, M., Ruszkiewicz, A., Timpson, P., and Samuel, M.S. (2020). Acute compressive stress activates RHO/ROCK-mediated cellular processes. Small GTPases *11*, 354–370.

Byrne, K.M., Monsefi, N., Dawson, J.C., Degasperi, A., Bukowski-Wills, J.C., Volinsky, N., Dobrzyński, M., Birtwistle, M.R., Tsyganov, M.A., Kiyatkin, A., et al. (2016). Bistability in the Rac1, PAK, and RhoA Signaling Network Drives Actin Cytoskeleton Dynamics and Cell Motility Switches. Cell Syst. *2*, 38–48.

Canel, M., Serrels, A., Miller, D., Timpson, P., Serrels, B., Frame, M.C., and Brunton, V.G. (2010). Quantitative in vivo imaging of the effects of inhibiting integrin signaling via Src and FAK on cancer cell movement: effects on E-cadherin dynamics. Cancer Res. *70*, 9413–9422.

Cardama, G.A., Comin, M.J., Hornos, L., Gonzalez, N., Defelipe, L., Turjanski, A.G., Alonso, D.F., Gomez, D.E., and Menna, P.L. (2014). Preclinical development of novel Rac1-GEF signaling inhibitors using a rational design approach in highly aggressive breast cancer cell lines. Anticancer. Agents Med. Chem. *14*, 840–851.

Cherfils, J., and Zeghouf, M. (2013). Regulation of small GTPases by GEFs, GAPs, and GDIs. Physiol. Rev. *93*, 269–309.

Colón-Bolea, P., García-Gómez, R., Shackleton, S., Crespo, P., Bustelo, X.R., and Casar, B. (2020). RAC1 induces nuclear alterations through the LINC complex to enhance melanoma invasiveness. Mol. Biol. Cell *31*, 2768–2778.

Conway, J.R.W., Carragher, N.O., and Timpson, P. (2014). Developments in preclinical cancer imaging: innovating the discovery of therapeutics. Nat. Rev. Cancer *14*, 314–328.

Conway, J.R.W., Warren, S.C., and Timpson, P. (2017). Context-dependent intravital imaging of therapeutic response using intramolecular FRET biosensors. Methods *128*, 78–94.

Conway, J.R.W., Warren, S.C., Herrmann, D., Murphy, K.J., Cazet, A.S., Vennin, C., Shearer, R.F., Killen, M.J., Magenau, A., Mélénec, P., et al. (2018). Intravital Imaging to Monitor Therapeutic Response in Moving Hypoxic Regions Resistant to PI3K Pathway Targeting in Pancreatic Cancer. Cell Rep. *23*, 3312–3326.

Cukierman, E., Pankov, R., Stevens, D.R., and Yamada, K.M. (2001). Taking cell-matrix adhesions to the third dimension. Science *294*, 1708–1712.

De, P., Aske, J.C., and Dey, N. (2019). RAC1 Takes the Lead in Solid Tumors. Cells *8*, 382.

Denais, C.M., Gilbert, R.M., Isermann, P., McGregor, A.L., Te Lindert, M., Weigelin, B., Davidson, P.M., Friedl, P., Wolf, K., and Lammerding, J. (2016). Nuclear envelope rupture and repair during cancer cell migration. Science *352*, 353–358.

Desmedt, C., Demicheli, R., Fornili, M., Bachir, I., Duca, M., Viglietti, G., Berlière, M., Piccart, M., Sotiriou, C., Sosnowski, M., et al. (2018). Potential Benefit of Intra-operative Administration of Ketorolac on Breast Cancer Recurrence According to the Patient's Body Mass Index. J. Natl. Cancer Inst. *110*, 1115–1122.

Du, J., Xu, R., Hu, Z., Tian, Y., Zhu, Y., Gu, L., and Zhou, L. (2011). PI3K and ERK-induced Rac1 activation mediates hypoxia-induced HIF-1α expression in MCF-7 breast cancer cells. PLoS ONE *6*, e25213.

Dull, T., Zufferey, R., Kelly, M., Mandel, R.J., Nguyen, M., Trono, D., and Naldini, L. (1998). A third-generation lentivirus vector with a conditional packaging system. J. Virol. *72*, 8463–8471.

Dütting, S., Heidenreich, J., Cherpokova, D., Amin, E., Zhang, S.C., Ahmadian, M.R., Brakebusch, C., and Nieswandt, B. (2015). Critical off-target effects of the widely used Rac1 inhibitors NSC23766 and EHT1864 in mouse platelets. J. Thromb. Haemost. *13*, 827–838.

Ebrahim, S., and Weigert, R. (2019). Intravital microscopy in mammalian multicellular organisms. Curr. Opin. Cell Biol. *59*, 97–103.

Eddy, R.J., Weidmann, M.D., Sharma, V.P., and Condeelis, J.S. (2017). Tumor Cell Invadopodia: Invasive Protrusions that Orchestrate Metastasis. Trends Cell Biol. *27*, 595–607.

Ellenbroek, S.I.J., and van Rheenen, J. (2014). Imaging hallmarks of cancer in living mice. Nat. Rev. Cancer *14*, 406–418.

Erami, Z., Herrmann, D., Warren, S.C., Nobis, M., McGhee, E.J., Lucas, M.C., Leung, W., Reischmann, N., Mrowinska, A., Schwarz, J.P., et al. (2016). Intravital FRAP Imaging using an E-cadherin-GFP Mouse Reveals Disease- and Drug-Dependent Dynamic Regulation of Cell-Cell Junctions in Live Tissue. Cell Rep. *14*, 152–167.

Feng, M., Bao, Y., Li, Z., Li, J., Gong, M., Lam, S., Wang, J., Marzese, D.M., Donovan, N., Tan, E.Y., et al. (2014). RASAL2 activates RAC1 to promote triple-negative breast cancer progression. J. Clin. Invest. *124*, 5291–5304.

Festy, F., Ameer-Beg, S.M., Ng, T., and Suhling, K. (2007). Imaging proteins in vivo using fluorescence lifetime microscopy. Mol. Biosyst. *3*, 381–391.

Flynn, R., Paz, K., Du, J., Reichenbach, D.K., Taylor, P.A., Panoskaltsis-Mortari, A., Vulic, A., Luznik, L., MacDonald, K.K.P., Hill, G.R., et al. (2016). Targeted Rho-associated kinase 2 inhibition suppresses murine and human chronic GVHD through a Stat3-dependent mechanism. Blood *127*, 2144–2154.

Follain, G., Osmani, N., Azevedo, A.S., Allio, G., Mercier, L., Karreman, M.A., Solecki, G., Garcia Leòn, M.J., Lefebvre, O., Fekonja, N., et al. (2018). Hemodynamic Forces Tune the Arrest, Adhesion, and Extravasation of Circulating Tumor Cells. Dev. Cell *45*, 33–52.e12.

Follain, G., Herrmann, D., Harlepp, S., Hyenne, V., Osmani, N., Warren, S.C., Timpson, P., and Goetz, J.G. (2020). Fluids and their mechanics in tumour transit: shaping metastasis. Nat. Rev. Cancer *20*, 107–124.

Forget, P., Bentin, C., Machiels, J.P., Berliere, M., Coulie, P.G., and De Kock, M. (2014). Intraoperative use of ketorolac or diclofenac is associated with improved disease-free survival and overall survival in conservative breast cancer surgery. Br. J. Anaesth. *113* (*Suppl 1*), i82–i87.

Fort, L., Batista, J.M., Thomason, P.A., Spence, H.J., Whitelaw, J.A., Tweedy, L., Greaves, J., Martin, K.J., Anderson, K.I., Brown, P., et al. (2018). Fam49/CYRI interacts with Rac1 and locally suppresses protrusions. Nat. Cell Biol. *20*, 1159–1171.

Friedl, P., and Alexander, S. (2011). Cancer invasion and the microenvironment: plasticity and reciprocity. Cell *147*, 992–1009.

Fruhwirth, G.O., Fernandes, L.P., Weitsman, G., Patel, G., Kelleher, M., Lawler, K., Brock, A., Poland, S.P., Matthews, D.R., Kéri, G., et al. (2011). How Förster resonance energy transfer imaging improves the understanding of protein interaction networks in cancer biology. ChemPhysChem *12*, 442–461.

Gao, Y., Dickerson, J.B., Guo, F., Zheng, J., and Zheng, Y. (2004). Rational design and characterization of a Rac GTPase-specific small molecule inhibitor. Proc. Natl. Acad. Sci. USA *101*, 7618–7623.

Gligorijevic, B., Kedrin, D., Segall, J.E., Condeelis, J., and van Rheenen, J. (2009). Dendra2 photoswitching through the Mammary Imaging Window. J. Vis. Exp. *28*, 3–5.

Grasso, S., Chapelle, J., Salemme, V., Aramu, S., Russo, I., Vitale, N., Verdun di Cantogno, L., Dallaglio, K., Castellano, I., Amici, A., et al. (2017). The scaffold protein p140Cap limits ERBB2-mediated breast cancer progression interfering with Rac GTPase-controlled circuitries. Nat. Commun. *8*, 14797.

Guo, Y., Kenney, S.R., Muller, C.Y., Adams, S., Rutledge, T., Romero, E., Murray-Krezan, C., Prekeris, R., Sklar, L.A., Hudson, L.G., and Wandinger-Ness, A. (2015a). R-ketorolac targets Cdc42 and Rac1 and alters ovarian cancer cell behaviors critical for invasion and metastasis. Mol. Cancer Ther. *14*, 2215–2227.

Guo, Y., Kenney, S.R., Cook, L., Adams, S.F., Rutledge, T., Romero, E., Oprea, T.I., Sklar, L.A., Bedrick, E., Wiggins, C.L., et al. (2015b). A Novel Pharmacologic Activity of Ketorolac for Therapeutic Benefit in Ovarian Cancer Patients. Clin. Cancer Res. *21*, 5064–5072.

Guy, C.T., Cardiff, R.D., and Muller, W.J. (1992a). Induction of mammary tumors by expression of polyomavirus middle T oncogene: a transgenic mouse model for metastatic disease. Mol. Cell. Biol. *12*, 954–961.

Guy, C.T., Webster, M.A., Schaller, M., Parsons, T.J., Cardiff, R.D., and Muller, W.J. (1992b). Expression of the neu protooncogene in the mammary epithelium of transgenic mice induces metastatic disease. Proc. Natl. Acad. Sci. USA *89*, 10578–10582.

Hall, A. (1998). Rho GTPases and the actin cytoskeleton. Science *279*, 509–514.

Hall, A., and Nobes, C.D. (2000). Rho GTPases: molecular switches that control the organization and dynamics of the actin cytoskeleton. Philos. Trans. R. Soc. Lond. B Biol. Sci. *355*, 965–970.

Herrmann, D., Conway, J.R.W., Vennin, C., Magenau, A., Hughes, W.E., Morton, J.P., and Timpson, P. (2014). Three-dimensional cancer models mimic cell-matrix interactions in the tumour microenvironment. Carcinogenesis *35*, 1671–1679.

Hervieu, A., Heuss, S.F., Zhang, C., Barrow-McGee, R., Joffre, C., Ménard, L., Clarke, P.A., and Kermorgant, S. (2020). A PI3K- and GTPase-independent Rac1-mTOR mechanism mediates MET-driven anchorage-independent cell growth but not migration. Sci. Signal. *13*, eaba8627.

Hirata, E., Yukinaga, H., Kamioka, Y., Arakawa, Y., Miyamoto, S., Okada, T., Sahai, E., and Matsuda, M. (2012). In vivo fluorescence resonance energy transfer imaging reveals differential activation of Rho-family GTPases in glioblastoma cell invasion. J. Cell Sci. *125*, 858–868.

Hirata, E., Girotti, M.R., Viros, A., Hooper, S., Spencer-Dene, B., Matsuda, M., Larkin, J., Marais, R., and Sahai, E. (2015). Intravital imaging reveals how BRAF inhibition generates drug-tolerant microenvironments with high integrin β1/FAK signaling. Cancer Cell *27*, 574–588.

Hiratsuka, T., Fujita, Y., Naoki, H., Aoki, K., Kamioka, Y., and Matsuda, M. (2015). Intercellular propagation of extracellular signal-regulated kinase activation revealed by in vivo imaging of mouse skin. eLife *4*, e05178.

Hirota, K., and Semenza, G.L. (2001). Rac1 activity is required for the activation of hypoxia-inducible factor 1. J. Biol. Chem. *276*, 21166–21172.

Hodgson, L., Spiering, D., Sabouri-Ghomi, M., Dagliyan, O., DerMardirossian, C., Danuser, G., and Hahn, K.M. (2016). FRET binding antenna reports spatiotemporal dynamics of GDI-Cdc42 GTPase interactions. Nat. Chem. Biol. *12*, 802–809.

Hoffmann, C., Mao, X., Brown-Clay, J., Moreau, F., Al Absi, A., Wurzer, H., Sousa, B., Schmitt, F., Berchem, G., Janji, B., and Thomas, C. (2018). Hypoxia promotes breast cancer cell invasion through HIF-1α-mediated up-regulation of the invadopodial actin bundling protein CSRP2. Sci. Rep. *8*, 10191.

Hou, H., Chávez, A.E., Wang, C.-C., Yang, H., Gu, H., Siddoway, B.A., Hall, B.J., Castillo, P.E., and Xia, H. (2014). The Rac1 inhibitor NSC23766 suppresses CREB signaling by targeting NMDA receptor function. J. Neurosci. *34*, 14006–14012.

Ingrao, J.C., Johnson, R., Tor, E., Gu, Y., Litman, M., and Turner, P.V. (2013). Aqueous stability and oral pharmacokinetics of meloxicam and carprofen in male C57BL/6 mice. J. Am. Assoc. Lab. Anim. Sci. *52*, 553–559.

Itoh, R.E., Kurokawa, K., Ohba, Y., Yoshizaki, H., Mochizuki, N., and Matsuda, M. (2002). Activation of rac and cdc42 video imaged by fluorescent resonance energy transfer-based single-molecule probes in the membrane of living cells. Mol. Cell. Biol. *22*, 6582–6591.

Janssen, A., Beerling, E., Medema, R., and van Rheenen, J. (2013). Intravital FRET imaging of tumor cell viability and mitosis during chemotherapy. PLoS ONE *8*, e64029.

Johnson, M.A., Sharma, M., Mok, M.T.S., and Henderson, B.R. (2013). Stimulation of in vivo nuclear transport dynamics of actin and its co-factors IQGAP1 and Rac1 in response to DNA replication stress. Biochim. Biophys. Acta *1833*, 2334–2347.

Johnsson, A.E., Dai, Y., Nobis, M., Baker, M.J., McGhee, E.J., Walker, S., Schwarz, J.P., Kadir, S., Morton, J.P., Myant, K.B., et al. (2014). The Rac-FRET mouse reveals tight spatiotemporal control of Rac activity in primary cells and tissues. Cell Rep. *6*, 1153–1164.

Katz, E., Sims, A.H., Sproul, D., Caldwell, H., Dixon, M.J., Meehan, R.R., and Harrison, D.J. (2012). Targeting of Rac GTPases blocks the spread of intact human breast cancer. Oncotarget *3*, 608–619.

Kawazu, M., Ueno, T., Kontani, K., Ogita, Y., Ando, M., Fukumura, K., Yamato, A., Soda, M., Takeuchi, K., Miki, Y., et al. (2013). Transforming mutations of RAC guanosine triphosphatases in human cancers. Proc. Natl. Acad. Sci. USA *110*, 3029–3034.

Kedrin, D., Gligorijevic, B., Wyckoff, J., Verkhusha, V.V., Condeelis, J., Segall, J.E., and van Rheenen, J. (2008). Intravital imaging of metastatic behavior through a mammary imaging window. Nat. Methods *5*, 1019–1021.

Komatsu, N., Fujita, Y., Matsuda, M., and Aoki, K. (2015). mTORC1 upregulation via ERK-dependent gene expression change confers intrinsic resistance to MEK inhibitors in oncogenic KRas-mutant cancer cells. Oncogene *34*, 5607–5616.

Kondo, H., Ratcliffe, C.D.H., Hooper, S., Ellis, J., MacRae, J.I., Hennequart, M., Dunsby, C.W., Anderson, K.I., and Sahai, E. (2021). Single-cell resolved imaging reveals intra-tumor heterogeneity in glycolysis, transitions between metabolic states, and their regulatory mechanisms. Cell Rep. *34*, 108750.

Kunschmann, T., Puder, S., Fischer, T., Steffen, A., Rottner, K., and Mierke, C.T. (2019). The Small GTPase Rac1 Increases Cell Surface Stiffness and Enhances 3D Migration Into Extracellular Matrices. Sci. Rep. *9*, 7675.

Lamm, N., Read, M.N., Nobis, M., Van Ly, D., Page, S.G., Masamsetti, V.P., Timpson, P., Biro, M., and Cesare, A.J. (2020). Nuclear F-actin counteracts nuclear deformation and promotes fork repair during replication stress. Nat. Cell Biol. *22*, 1460–1470.

Lawson, C.D., and Burridge, K. (2014). The on-off relationship of Rho and Rac during integrin-mediated adhesion and cell migration. Small GTPases *5*, e27958.

Lehmann, S., Te Boekhorst, V., Odenthal, J., Bianchi, R., van Helvert, S., Ikenberg, K., Ilina, O., Stoma, S., Xandry, J., Jiang, L., et al. (2017). Hypoxia Induces a HIF-1-Dependent Transition from Collective-to-Amoeboid Dissemination in Epithelial Cancer Cells. Curr. Biol. *27*, 392–400.

Levay, M., Krobert, K.A., Wittig, K., Voigt, N., Bermudez, M., Wolber, G., Dobrev, D., Levy, F.O., and Wieland, T. (2013). NSC23766, a widely used inhibitor of Rac1 activation, additionally acts as a competitive antagonist at muscarinic acetylcholine receptors. J. Pharmacol. Exp. Ther. *347*, 69–79.

Li, Z., Liu, Q., Piao, J., Hua, F., Wang, J., Jin, G., Lin, Z., and Zhang, Y. (2016). Clinicopathological implications of Tiam1 overexpression in invasive ductal carcinoma of the breast. BMC Cancer *16*, 681.

Liao, D., Corle, C., Seagroves, T.N., and Johnson, R.S. (2007). Hypoxia-inducible factor-1alpha is a key regulator of metastasis in a transgenic model of cancer initiation and progression. Cancer Res. *67*, 563–572.

Lin, E.Y., Jones, J.G., Li, P., Zhu, L., Whitney, K.D., Muller, W.J., and Pollard, J.W. (2003). Progression to malignancy in the polyoma middle T oncoprotein mouse breast cancer model provides a reliable model for human diseases. Am. J. Pathol. *163*, 2113–2126.

Lindsay, C.R., Lawn, S., Campbell, A.D., Faller, W.J., Rambow, F., Mort, R.L., Timpson, P., Li, A., Cammareri, P., Ridgway, R.A., et al. (2011). P-Rex1 is required for efficient melanoblast migration and melanoma metastasis. Nat. Commun. *2*, 555.

Liu, H.-J., Ooms, L.M., Srijakotre, N., Man, J., Vieusseux, J., Waters, J.E., Feng, Y., Bailey, C.G., Rasko, J.E.J., Price, J.T., and Mitchell, C.A. (2016). PtdIns(3,4,5)P3-dependent Rac Exchanger 1 (PREX1) Rac-Guanine Nucleotide Exchange Factor (GEF) Activity Promotes Breast Cancer Cell Proliferation and Tumor Growth via Activation of Extracellular Signal-regulated Kinase 1/2 (ERK1/2) Signaling. J. Biol. Chem. *291*, 17258–17270.

Lomakin, A.J., Cattin, C.J., Cuvelier, D., Alraies, Z., Molina, M., Nader, G.P.F., Srivastava, N., Saez, P.J., Garcia-Arcos, J.M., Zhitnyak, I.Y., et al. (2020). The

nucleus acts as a ruler tailoring cell responses to spatial constraints. Science *370*, eaba2894.

Machacek, M., Hodgson, L., Welch, C., Elliott, H., Pertz, O., Nalbant, P., Abell, A., Johnson, G.L., Hahn, K.M., and Danuser, G. (2009). Coordination of Rho GTPase activities during cell protrusion. Nature *461*, 99–103.

Machesky, L.M., and Insall, R.H. (1998). Scar1 and the related Wiskott-Aldrich syndrome protein, WASP, regulate the actin cytoskeleton through the Arp2/3 complex. Curr. Biol. *8*, 1347–1356.

Machesky, L.M., and Sansom, O.J. (2012). Rac1 in the driver's seat for melanoma. Pigment Cell Melanoma Res. *25*, 762–764.

Mack, N.A., Porter, A.P., Whalley, H.J., Schwarz, J.P., Jones, R.C., Khaja, A.S.S., Bjartell, A., Anderson, K.I., and Malliri, A. (2012). β2-syntrophin and Par-3 promote an apicobasal Rac activity gradient at cell-cell junctions by differentially regulating Tiam1 activity. Nat. Cell Biol. *14*, 1169–1180.

Macpherson, I.R., Rainero, E., Mitchell, L.E., van den Berghe, P.V.E., Speirs, C., Dozynkiewicz, M.A., Chaudhary, S., Kalna, G., Edwards, J., Timpson, P., and Norman, J.C. (2014). CLIC3 controls recycling of late endosomal MT1-MMP and dictates invasion and metastasis in breast cancer. J. Cell Sci. *127*, 3893–3901.

Malliri, A., van der Kammen, R.A., Clark, K., van der Valk, M., Michiels, F., and Collard, J.G. (2002). Mice deficient in the Rac activator Tiam1 are resistant to Ras-induced skin tumours. Nature *417*, 867–871.

Marei, H., and Malliri, A. (2017). Rac1 in human diseases: The therapeutic potential of targeting Rac1 signaling regulatory mechanisms. Small GTPases *8*, 139–163.

Marei, H., Carpy, A., Woroniuk, A., Vennin, C., White, G., Timpson, P., Macek, B., and Malliri, A. (2016). Differential Rac1 signalling by guanine nucleotide exchange factors implicates FLII in regulating Rac1-driven cell migration. Nat. Commun. *7*, 10664.

Matsuda, M., and Terai, K. (2020). Experimental pathology by intravital microscopy and genetically encoded fluorescent biosensors. Pathol. Int. *70*, 379–390.

Miller, M.A., and Weissleder, R. (2017). Imaging of anticancer drug action in single cells. Nat. Rev. Cancer *17*, 399–414.

Mills, S.C., Howell, L., Beekman, A., Stokes, L., and Mueller, A. (2018). Rac1 plays a role in CXCL12 but not CCL3-induced chemotaxis and Rac1 GEF inhibitor NSC23766 has off target effects on CXCR4. Cell. Signal. *42*, 88–96.

Montalvo-Ortiz, B.L., Castillo-Pichardo, L., Hernández, E., Humphries-Bickley, T., De la Mota-Peynado, A., Cubano, L.A., Vlaar, C.P., and Dharmawardhane, S. (2012). Characterization of EHop-016, novel small molecule inhibitor of Rac GTPase. J. Biol. Chem. *287*, 13228–13238.

Moose, D.L., Krog, B.L., Kim, T.-H., Zhao, L., Williams-Perez, S., Burke, G., Rhodes, L., Vanneste, M., Breheny, P., Milhem, M., et al. (2020). Cancer Cells Resist Mechanical Destruction in Circulation via RhoA/Actomyosin-Dependent Mechano-Adaptation. Cell Rep. *30*, 3864–3874.e6.

Moshfegh, Y., Bravo-Cordero, J.J., Miskolci, V., Condeelis, J., and Hodgson, L. (2014). A Trio-Rac1-Pak1 signalling axis drives invadopodia disassembly. Nat. Cell Biol. *16*, 574–586.

Munro, J., Steeghs, K., Morrison, V., Ireland, H., and Parkinson, E.K. (2001). Human fibroblast replicative senescence can occur in the absence of extensive cell division and short telomeres. Oncogene *20*, 3541–3552.

Myant, K.B., Cammareri, P., McGhee, E.J., Ridgway, R.A., Huels, D.J., Cordero, J.B., Schwitalla, S., Kalna, G., Ogg, E.L., Athineos, D., et al. (2013). ROS production and NF-κB activation triggered by RAC1 facilitate WNT-driven intestinal stem cell proliferation and colorectal cancer initiation. Cell Stem Cell *12*, 761–773.

Newman, R.H., Fosbrink, M.D., and Zhang, J. (2011). Genetically encodable fluorescent biosensors for tracking signaling dynamics in living cells. Chem. Rev. *111*, 3614–3666.

Nobes, C.D., and Hall, A. (1995). Rho, rac, and cdc42 GTPases regulate the assembly of multimolecular focal complexes associated with actin stress fibers, lamellipodia, and filopodia. Cell *81*, 53–62.

Nobis, M., McGhee, E.J., Morton, J.P., Schwarz, J.P., Karim, S.A., Quinn, J., Edward, M., Campbell, A.D., McGarry, L.C., Evans, T.R.J., et al. (2013). Intravital FLIM-FRET imaging reveals dasatinib-induced spatial control of src in pancreatic cancer. Cancer Res. *73*, 4674–4686.

Nobis, M., Herrmann, D., Warren, S.C., Kadir, S., Leung, W., Killen, M., Magenau, A., Stevenson, D., Lucas, M.C., Reischmann, N., et al. (2017). A RhoA-FRET Biosensor Mouse for Intravital Imaging in Normal Tissue Homeostasis and Disease Contexts. Cell Rep. *21*, 274–288.

Nobis, M., Warren, S.C., Lucas, M.C., Murphy, K.J., Herrmann, D., and Timpson, P. (2018). Molecular mobility and activity in an intravital imaging setting - implications for cancer progression and targeting. J. Cell Sci. *131*, jcs206995.

Nobis, M., Herrmann, D., Warren, S.C., Strathdee, D., Cox, T.R., Anderson, K.I., and Timpson, P. (2020). Shedding new light on RhoA signalling as a drug target in vivo using a novel RhoA-FRET biosensor mouse. Small GTPases *21*, 1–8.

Oprea, T.I., Sklar, L.A., Agola, J.O., Guo, Y., Silberberg, M., Roxby, J., Vestling, A., Romero, E., Surviladze, Z., Murray-Krezan, C., et al. (2015). Novel Activities of Select NSAID R-Enantiomers against Rac1 and Cdc42 GTPases. PLoS ONE *10*, e0142182.

Retsky, M., Rogers, R., Demicheli, R., Hrushesky, W.J.M., Gukas, I., Vaidya, J.S., Baum, M., Forget, P., Dekock, M., and Pachmann, K. (2012). NSAID analgesic ketorolac used perioperatively may suppress early breast cancer relapse: particular relevance to triple negative subgroup. Breast Cancer Res. Treat. *134*, 881–888.

Ridley, A.J. (2015). Rho GTPase signalling in cell migration. Curr. Opin. Cell Biol. *36*, 103–112.

Ridley, A.J., and Hall, A. (1992). The small GTP-binding protein rho regulates the assembly of focal adhesions and actin stress fibers in response to growth factors. Cell *70*, 389–399.

Ridley, A.J., Paterson, H.F., Johnston, C.L., Diekmann, D., and Hall, A. (1992). The small GTP-binding protein rac regulates growth factor-induced membrane ruffling. Cell *70*, 401–410.

Ritsma, L., Steller, E.J.A., Beerling, E., Loomans, C.J.M., Zomer, A., Gerlach, C., Vrisekoop, N., Seinstra, D., van Gurp, L., Schäfer, R., et al. (2012). Intravital microscopy through an abdominal imaging window reveals a pre-micrometastasis stage during liver metastasis. Sci. Transl. Med. *4*, 158ra145.

Ritsma, L., Steller, E.J.A., Ellenbroek, S.I.J., Kranenburg, O., Borel Rinkes, I.H.M., and van Rheenen, J. (2013). Surgical implantation of an abdominal imaging window for intravital microscopy. Nat. Protoc. *8*, 583–594.

Ritsma, L., Ellenbroek, S.I.J., Zomer, A., Snippert, H.J., de Sauvage, F.J., Simons, B.D., Clevers, H., and van Rheenen, J. (2014). Intestinal crypt homeostasis revealed at single-stem-cell level by in vivo live imaging. Nature *507*, 362–365.

Roebroek, T., Vandenberg, W., Sipieter, F., Hugelier, S., Stove, C., Zhang, J., and Dedecker, P. (2021). Simultaneous readout of multiple FRET pairs using photochromism. Nat. Commun. *12*, 2005.

Samuel, M.S., Lourenço, F.C., and Olson, M.F. (2011). K-Ras mediated murine epidermal tumorigenesis is dependent upon and associated with elevated Rac1 activity. PLoS ONE *6*, e17143.

Scheele, C.L.G.J., Maynard, C., and van Rheenen, J. (2016). Intravital Insights into Heterogeneity, Metastasis, and Therapy Responses. Trends Cancer *2*, 205–216.

Schnelzer, A., Prechtel, D., Knaus, U., Dehne, K., Gerhard, M., Graeff, H., Harbeck, N., Schmitt, M., and Lengyel, E. (2000). Rac1 in human breast cancer: overexpression, mutation analysis, and characterization of a new isoform, Rac1b. Oncogene *19*, 3013–3020.

Shcherbakova, D.M., Cox Cammer, N., Huisman, T.M., Verkhusha, V.V., and Hodgson, L. (2018). Direct multiplex imaging and optogenetics of Rho GTPases enabled by near-infrared FRET. Nat. Chem. Biol. *14*, 591–600.

Shutes, A., Onesto, C., Picard, V., Leblond, B., Schweighoffer, F., and Der, C.J. (2007). Specificity and mechanism of action of EHT 1864, a novel small molecule inhibitor of Rac family small GTPases. J. Biol. Chem. *282*, 35666–35678.

Siegel, R.L., Miller, K.D., and Jemal, A. (2020). Cancer statistics, 2020. CA Cancer J. Clin. *70*, 7–30.

Sosa, M.S., Lopez-Haber, C., Yang, C., Wang, H., Lemmon, M.A., Busillo, J.M., Luo, J., Benovic, J.L., Klein-Szanto, A., Yagi, H., et al. (2010). Identification of the Rac-GEF P-Rex1 as an essential mediator of ErbB signaling in breast cancer. Mol. Cell *40*, 877–892.

Spence, H.J., Timpson, P., Tang, H.R., Insall, R.H., and Machesky, L.M. (2012). Scar/WAVE3 contributes to motility and plasticity of lamellipodial dynamics but not invasion in three dimensions. Biochem. J. *448*, 35–42.

Spiering, D., and Hodgson, L. (2011). Dynamics of the Rho-family small GTPases in actin regulation and motility. Cell Adhes. Migr. *5*, 170–180.

Srijakotre, N., Liu, H.-J., Nobis, M., Man, J., Yip, H.Y.K., Papa, A., Abud, H.E., Anderson, K.I., Welch, H.C.E., Tiganis, T., et al. (2020). PtdIns(3,4,5)P_3-dependent Rac exchanger 1 (P-Rex1) promotes mammary tumor initiation and metastasis. Proc. Natl. Acad. Sci. USA *117*, 28056–28067.

Steeg, P.S. (2016). Targeting metastasis. Nat. Rev. Cancer *16*, 201–218.

Thiam, H.-R., Vargas, P., Carpi, N., Crespo, C.L., Raab, M., Terriac, E., King, M.C., Jacobelli, J., Alberts, A.S., Stradal, T., et al. (2016). Perinuclear Arp2/3-driven actin polymerization enables nuclear deformation to facilitate cell migration through complex environments. Nat. Commun. *7*, 10997.

Timpson, P., Jones, G.E., Frame, M.C., and Brunton, V.G. (2001). Coordination of cell polarization and migration by the Rho family GTPases requires Src tyrosine kinase activity. Curr. Biol. *11*, 1836–1846.

Timpson, P., McGhee, E.J., Morton, J.P., von Kriegsheim, A., Schwarz, J.P., Karim, S.A., Doyle, B., Quinn, J.A., Carragher, N.O., Edward, M., et al. (2011a). Spatial regulation of RhoA activity during pancreatic cancer cell invasion driven by mutant p53. Cancer Res. *71*, 747–757.

Timpson, P., McGhee, E.J., Erami, Z., Nobis, M., Quinn, J.A., Edward, M., and Anderson, K.I. (2011b). Organotypic collagen I assay: a malleable platform to assess cell behaviour in a 3-dimensional context. J. Vis. Exp. *56*, e3089.

Vega, F.M., and Ridley, A.J. (2008). Rho GTPases in cancer cell biology. FEBS Lett. *582*, 2093–2101.

Vennin, C., Herrmann, D., Lucas, M.C., and Timpson, P. (2016). Intravital imaging reveals new ancillary mechanisms co-opted by cancer cells to drive tumor progression. F1000Res. *5*, 1–12.

Vennin, C., Chin, V.T., Warren, S.C., Lucas, M.C., Herrmann, D., Magenau, A., Melenec, P., Walters, S.N., Del Monte-Nieto, G., Conway, J.R.W., et al.; Australian Pancreatic Cancer Genome Initiative (APGI) (2017). Transient tissue priming via ROCK inhibition uncouples pancreatic cancer progression, sensitivity to chemotherapy, and metastasis. Sci. Transl. Med. *9*, eaai8504.

Vennin, C., Mélénec, P., Rouet, R., Nobis, M., Cazet, A.S., Murphy, K.J., Herrmann, D., Reed, D.A., Lucas, M.C., Warren, S.C., et al.; Australian Pancreatic Genome Initiative (APGI) (2019). CAF hierarchy driven by pancreatic cancer cell p53-status creates a pro-metastatic and chemoresistant environment via perlecan. Nat. Commun. *10*, 3637.

Venturini, V., Pezzano, F., Castro, F.C., Häkkinen, H.M., Jiménez-Delgado, S., Colomer-Rosell, M., Marro, M., Tolosa-Ramon, Q., Paz-López, S., Valverde, M.A., et al. (2020). The nucleus measures shape changes for cellular proprioception to control dynamic cell behavior. Science *370*, eaba2644.

Wang, Y., Bibi, M., Min, P., Deng, W., Zhang, Y., and Du, J. (2019). SOX2 promotes hypoxia-induced breast cancer cell migration by inducing NEDD9 expression and subsequent activation of Rac1/HIF-1α signaling. Cell. Mol. Biol. Lett. *24*, 55.

Warren, S.C., Nobis, M., Magenau, A., Mohammed, Y.H., Herrmann, D., Moran, I., Vennin, C., Conway, J.R., Mélénec, P., Cox, T.R., et al. (2018). Removing physiological motion from intravital and clinical functional imaging data. eLife *7*, 1–37.

Welch, H.C.E., Condliffe, A.M., Milne, L.J., Ferguson, G.J., Hill, K., Webb, L.M.C., Okkenhaug, K., Coadwell, W.J., Andrews, S.R., Thelen, M., et al. (2005). P-Rex1 regulates neutrophil function. Curr. Biol. *15*, 1867–1873.

Woodcock, S.A., Rooney, C., Liontos, M., Connolly, Y., Zoumpourlis, V., Whetton, A.D., Gorgoulis, V.G., and Malliri, A. (2009). SRC-induced disassembly of adherens junctions requires localized phosphorylation and degradation of the rac activator tiam1. Mol. Cell *33*, 639–653.

Woroniuk, A., Porter, A., White, G., Newman, D.T., Diamantopoulou, Z., Waring, T., Rooney, C., Strathdee, D., Marston, D.J., Hahn, K.M., et al. (2018). STEF/TIAM2-mediated Rac1 activity at the nuclear envelope regulates the perinuclear actin cap. Nat. Commun. *9*, 2124.

Yamaguchi, H., and Condeelis, J. (2007). Regulation of the actin cytoskeleton in cancer cell migration and invasion. Biochim. Biophys. Acta *1773*, 642–652.

Yamaguchi, M., Takagi, K., Sato, A., Miki, Y., Miyashita, M., Sasano, H., and Suzuki, T. (2020). Rac1 activation in human breast carcinoma as a prognostic factor associated with therapeutic resistance. Breast Cancer *27*, 919–928.

Yoshida, T., Zhang, Y., Rivera Rosado, L.A., Chen, J., Khan, T., Moon, S.Y., and Zhang, B. (2010). Blockade of Rac1 activity induces G1 cell cycle arrest or apoptosis in breast cancer cells through downregulation of cyclin D1, survivin, and X-linked inhibitor of apoptosis protein. Mol. Cancer Ther. *9*, 1657–1668.

Young, A.I.J., Law, A.M.K., Castillo, L., Chong, S., Cullen, H.D., Koehler, M., Herzog, S., Brummer, T., Lee, E.F., Fairlie, W.D., et al. (2016). MCL-1 inhibition provides a new way to suppress breast cancer metastasis and increase sensitivity to dasatinib. Breast Cancer Res. *18*, 125.

Zhong, Y., Zhang, J., Zhou, Y., Mao, F., Lin, Y., Xu, Y., Guan, J., Shen, S., Pan, B., Wang, C., et al. (2019). Phosphatidylinositol-3,4,5-Trisphosphate Dependent Rac Exchange Factor 1 (PREX1) is a Novel Predictor of Prognosis for Breast Cancer Patients: A Retrospective Case Series. Med. Sci. Monit. *25*, 6554–6562.

STAR★METHODS

KEY RESOURCES TABLE

Reagent or Resource	Source	Identifier
Antibodies		
Mouse monoclonal IgG1 anti-Rac1	Cytoskeleton	Cat# ARC03, RRID:AB_10709099
Rabbit poly-clonal IgG anti-GFP	Abcam	Cat# ab290, RRID:AB_303395
Rabbit monoclonal IgG1 anti-GAPDH	Cell Signaling	Cat# 2118, RRID:AB_561053
Sheep-anti-Mouse IgG HRP-linked	GE healthcare	Cat# NA931, RRID:AB_772210
Donkey-anti-Rabbit IgG HRP-linked	GE healthcare	Cat# NA934, RRID:AB_772206
Rabbit monoclonal IgG1 anti-Ki67	ThermoFisher Scientific	Cat# RM-9106-S1, RRID:AB_149792
Rabbit polyclonal anti-cleaved Caspase-3	Cell Signaling	Cat# 9661, RRID:AB_2341188
Rabbit monoclonal anti-Cyclin B1 (EPR17060)	Abcam	Cat# ab181593, RRID:AB_2820245
Rabbit polyclonal anti- Cyclin A2 (C-19)	Santa Cruz Biotechnology	Cat# sc-596
Rabbit polyclonal anti-PAK1	Cell Signaling	Cat# 2602, RRID:AB_330222
Rabbit polyclonal anti-PAK1 (Ser199/204)/PAK2 (Ser192/197)	Cell Signaling	Cat# 2605, RRID:AB_2160222
Mouse Monoclonal anti-beta-actin (clone AC-15)	Merck (SigmaAldrich)	Cat# A5441, RRID:AB_476744
Bacterial and virus strains		
E. coli DH5α	ThermoFisher Scientific	Cat# 18265017
Chemicals, peptides and recombinant proteins		
Qtracker 655 Vascular Label	ThermoFisher Scientific	Cat# Q21021MP
AnnexinV-Cy5	BioVision	Cat# 1013
Propidium iodide	Merck, Sigma-Aldrich	Cat# P4170
SalI	Promega	Cat# R6051
NdeI	New England Biolabs	Cat# R0111S
Rac1 Pull-down Activation Assay Biochem Kit	CytoSkeleton Inc.	Cat# BK035
Experimental models: Cell lines		
PyMT 20065 (from mouse 20065, female)	SEARCHBreast	https://searchbreast.org/
MMTV-PyMT;Rac1-FRET (from mouse 8625, female)	This study	N/A
MMTV-PyMT;Rac1-FRET;P-Rex1 ± (from mouse 138509, female)	This study	N/A
Experimental models: Organisms/strains		
Rac1-FRET mice (ubiquitously expressed, "ON")	Prof. Heidi CE Welch, Babraham Institute, UK, Johnsson et al. 2014	N/A
MMTV-Her2 mice	The Jackson Laboratory	Stock# 002376
MMTV-PyMT mice	The Jackson Laboratory	Stock# 002374
K14-CreER mice	The Jackson Laboratory	Stock# 005107
LSL-K-Ras G12D mice	The Jackson Laboratory	Stock# 008179
Rac1-flox mice	Prof L. Machesky, Prof O. Sansom, CRUK Beatson Institute, University of Glasgow	N/A
P-Rex1 KO mice	Prof. Heidi CE Welch, Babraham Institute, UK, Welch et al. 2005	N/A
FVB/NJ (Ausb) mice	The Jackson Laboratory	Stock# 001800
NOD.Cg-Prkdc < scid > IL2rg < tm1Wjl > /SzJ (Ausb) mice	The Jackson Laboratory	Stock# 005557
BALB/c-Fox1nu (Ausb) mice	Charles River	Strain# 194

(*Continued on next page*)

Continued

Reagent or Resource	Source	Identifier
Oligonucleotides		
Primer: piggy- 3terminalR GGTCTGTATATCGAGGTTTAT	This study	N/A
Primer: piggy- 5terminalF ACTATAACGACCGCGTGAG	This study	N/A
Recombinant DNA		
pDendra2-C	Evrogen	Cat# FP821
pMCV-hyPBase	Sanger Institute	N/A
pPB-Cag.EBNXN	Sanger Institute	N/A
pPB-CAG-Dendra2-C	This study	N/A
pLV430G-ofI-2TA-EGFP	A kind gift from Dr Bian Rabinovich, The University of Texas M. D. Anderson Cancer Center, USA	N/A
pMD2.G	Trono Lab Packaging and Envelope Plasmids (unpublished)	Addgene #12259
pRVS-Rev	Dull et al., 1998	Addgene #12253
pMDLg/pRRE	Dull et al., 1998	Addgene #12251
pCGN-P-Rex1-HA	A kind gift from Dr Lisa Ooms/ Prof Christina Mitchell, Monash University, Australia	N/A
pcDNA.3-Tiam1-HA	A kind gift from Prof Angeliki Malliri, CRUK Manchester Institute, University of Manchester, UK	N/A
pLHCX-CYRI-B-FLAG	A kind gift from Prof Laura Machesky, CRUK Beatson Institute, University of Glasgow, UK	N/A
pNice-HA-alpha2-Chimaerin	Beg et al., 2007	Addgene #59315
Software and algorithms		
FLIMFit v5.1.1.	Github/FLIMfit	https://flimfit.org/
Galene v2.2.0	GitHub	https://github.com/flimfit/Galene/releases/tag/2.2.0
ImspectorPro v2.5.0.0	LaVision Biotech	https://www.lavisionbiotec.com/
ImageJ	NIH	https://imagej.nih.gov/ij/
QuPath v0.2.0-m8	Github	https://qupath.github.io/
FlowJo v7.6	Tree Star Inc.	https://www.flowjo.com/
Prism 8	GraphPad	https://www.graphpad.com

RESOURCE AVAILABILITY

Lead contact

Further information and requests for resources and reagents should be directed to, and will be fulfilled by the corresponding author and Lead Contact, Max Nobis (m.nobis@garvan.org.au).

Materials availability

All unique/stable reagents generated in this study are available from the Lead Contact with a completed Materials Transfer Agreement.

Data and code availability

The published article includes all data generated or analyzed during this study. All data reported in this paper will be shared by the lead contact upon reasonable request. This paper does not report original code. Any additional information required to reanalyze the data reported in this paper is available from the lead contact upon request.

EXPERIMENTAL MODEL AND SUBJECT DETAILS

Animal models

Animal experiments were conducted in accordance with the Australian code of practice for care and use of animals for scientific purposes, in compliance with the Garvan/St Vincents Animal Ethics Committee guidelines (ARA 16/13, 19/13) and in compliance with the UK Home office guidelines under PPL 60/4264, respectively. FVB/NJAusb mice (imported to the Australian BioResource (ABR) from The Jackson Laboratory in 2014), BALB/c-Fox1nuAusb (received by the Australian BioResource from the University of New South Wales in 2008), Rac1-FRET (kindly provided by Prof Heidi CE Welch; Johnsson et al., 2014), MMTV-PyMT (The Jackson Laboratory; Guy et al., 1992a), MMTV-Her2 (The Jackson Laboratory; Guy et al., 1992b), P-Rex1 KO mice (kindly provided by Prof Heidi CE Welch; Welch et al., 2005) and K14-CreER;LSL-KRasG12D;Rac1+/− (kindly provided by Prof Mike Olson; Samuel et al., 2011) were kept in IVC isolator cages on a 12h light/dark cycle and fed *ad libitum*. After acclimatisation for at least seven days, 7 to 9 week old female BALB/c-Fox1nuAusb mice were injected in the inguinal mammary fat pad with 100 μL of a suspension of 2×10^6 PyMT 20065 Dendra2 tumor cells in Hank's balanced salt solution (HBSS, GIBCO). Orthotopic tumors were grown for 53 ± 2 days to generate fully formed primary tumors. Mice were then weighed every day until regaining pre-surgical weight and once weekly afterward until a primary tumor at the site of injection was visible or palpable. Mice were then weighed three times a week and the tumor was measured using callipers. For the survival experiment MMTV-PyMT;Rac1-FRET mice were enrolled on treatment at an average tumor size of 24.9 ± 12.7 mm^3. For lung colonization experiments 7 to 9 week old female FVB/NJAusb mice were injected i.v. with 1×10^6 syngeneic PyMT 20065 luciferase cells or 7 to 9 week old female NOD.Cg-Prkdc < scid > IL2rg < tm1Wjl > / SzJAusb mice with 1×10^6 MMTV-PyMT;Rac1-FRET cells to monitor late and early metastasis respectively.

Cell culture

MMTV-PyMT;Rac1-FRET cells, MMTV-PyMT;Rac1-FRET;P-Rex1$^{+/-}$ and PyMT 20065 cells were maintained in DMEM (Dulbecco's modified Eagle medium, GIBCO, Cat#: 11995-065 containing 25 mM Glucose, 40 μM Phenol Red, 4 mM L-Glutamine, 1 mM Sodium Pyruvate) supplemented with 10% FBS, 1% penicillin/streptomycin (P/S), 5 μg/mL insulin, 10 ng/mL epidermal growth factor (EGF) and 10 ng/mL Cholera Toxin A and Telomerase-immortalized fibroblasts (TIFs) in DMEM, 10% FBS, 1% P/S at 37°C and 5% CO_2. Cell lines were checked and confirmed free of mycoplasma.

METHOD DETAILS

Plasmid constructs

Dendra2 was cloned into a PiggyBac mediated transposon backbone plasmid pPB-Cag.EBNXN via restriction digest of the vectors with SalI (Promega) and NdeI (New England Biolabs) and overnight ligation of the isolated fragments using T4 ligase (New England Biolabs). Ampicillin resistant positive clones were picked, analyzed by sequencing using the following primers: piggy- 3terminalR: 'GGTCTGTATATCGAGGTTTAT'; piggy- 5terminalF: 'ACTATAACGACCGCGTGAG' and amplified using QIAmp DNA Midi Kits (QIAGEN).

Transient transfections and stable cell line establishment

For validation experiments MMTV-PyMT;Rac1-FRET cells were transfected with either pCGN-P-Rex1-HA (kind gift from Dr Lisa Ooms/Prof Christina Mitchell), pcDNA.3-Tiam1-HA (kind gift from Prof Angeliki Malliri), pLHCX-CYRI-B-FLAG (kind gift from Prof Laura Machesky) or pNice-HA-alpha2-Chimaerin (kind gift from Prof Peter Scheiffele, Addgene plasmid # 59315) Lipofectamine™ 3000 Reagent as per the manufacturers' instructions.

In order to establish a PyMT 20065 Dendra2 cell line, PyMT 20065 cells were transfected using Lipofectamine™ 3000 Reagent as per the manufacturers' instructions. Briefly, 5 μg DNA (at a ratio of 1:3 of the pPB-CAG-Dendra2-C and pCMV-hyPBase plasmids) were mixed with 10 μL P3000™ Reagent in 250 μL Opti-MEM™ medium and the lipofectamine. Following an incubation at 37°C for 15 min the mixture was added to the cells in a 6 well dish and incubated overnight. Stable pools of cells expressing Dendra2 were established by FACS sorting (BD FACS Aria II).

To establish a PyMT 20065-luciferase cell line, lentiviral vectors were produced in HEK293T cells as described previously (Vennin et al., 2017). HEK293T cells were seeded at a density of 2×10^6 cells per 10 cm^2 dish. The following day the cells were transfected using the calcium phosphate-mediated transfection with helper plasmids encoding for viral envelope glycoprotein VSV-G in pMD2.G and packaging proteins gag, pol, rev and tat in psPAX2 and the target construct in pLV430G-ofI-2TA-EGFP. On the third day, the medium was replaced on the transfected cells with 6 mL of DMEM, 20% FBS, 1% P/S. On the same day recipient PyMT 20065 cells were seeded at a density of 1×10^5 cells per well in a 6 well dish. After overnight incubation viral particles were harvested, passed through a 0.45 μm filter and added to the PyMT cells supplemented with 10 ng/mL polybrene. To generate stable pools cells were FACS sorted using the EGFP expression.

In order to generate MMTV-PyMT;Rac1-FRET;CYRI-B cells, Phoenix-AMPHO cells were seeded at a density of 2×10^6 cells per 10 cm^2 dish and were transfected using the calcium phosphate-mediated transfection with the pLHCX-CYRI-B-FLAG plasmid. The medium was replaced on the transfected cells with 6 mL of DMEM, 20% FBS, 1% P/S the following day. On the same day recipient

MMTV-PyMT;Rac1-FRET cells were seeded at a density of 1 × 10^5 cells per well in a 6 well dish. After overnight incubation viral particles were harvested, passed through a 0.45 μm filter and added to the PyMT cells supplemented with 10 ng/mL polybrene. Stable pools were generated by selection with 500 μg/mL hygromycin.

2D Scratch Assay

MMTV-PyMT;Rac1-FRET were seeded at a density of 10,000 per well in a 96 well format and allowed to reach confluency overnight. The next day using a Woundmaker96 (Essen Bioscience) a scratch wound was made in each well and the wells treated in sextuplicate with ± DMSO, 20 μM EHT 1864 and 50 μM NSC 23766 and imaged every 2 h for up to 48 h on an IncuCyte Zoom Kinetic Imaging System (Essen Bioscience). The area of the wound was measured in ImageJ (NIH) and plotted and analyzed in Prism 8 (GraphPad).

Organotypic Invasion

3D organotypic invasion assays were set up as described previously (Nobis et al., 2013; Timpson et al., 2011b; Vennin et al., 2017). Briefly, collagen was isolated from 12 to 14 frozen adolescent rat tails by extraction of the tendons into 1.5 L pre-cooled 0.5 M acetic acid keeping the mixture under stirring at 4°C for 48 - 72 h. Remaining sheaths were removed by filtering the collagen extract through a mesh towel before the addition of 10% (w/v) NaCl to precipitate the collagen. After stirring for 30 to 60 min to obtain a homogeneous mixture, the extract was then centrifuged for 30 min at 10,000 rpm. The precipitate was then re-dissolved in 300 mL of 0.25 M pre-cooled acetic acid by stirring at 4°C for 24 h. Subsequent dialysis was performed against six to eight changes of 5 L Millipore water containing 17.5 mM acetic acid. The collagen was centrifuged at 14,000 rpm for 1.5 h and the supernatant was placed in a sterile flask and stored at 4°C. For approximately 12 organotypic matrices, 25 mL collagen was mixed with 3 mL MEM 10x media (GIBCO) and neutralized by titration of 0.22 M NaOH. Telomerase-immortalized fibroblasts (TIFs; Munro et al., 2001) were resuspended in 3 mL FBS and added to the collagen mixture. 2.5 mL of this collagen/fibroblast mix per matrix was then plated in 6-well culture dishes and allowed to solidify for 30 min at 37°C and 5% CO_2. 1 mL of basic growth medium was added per well and the matrices detached to contract freely. The organotypic matrices were allowed to contract for approximately 10-14 days at 37°C and 5% CO_2, while the media was changed every second day. The organotypic matrices were cleared of the fibroblasts by the addition of 10 μg/mL Puromycin to the medium for three days and subsequent washing of the matrices with PBS three times. MMTV-PyMT;Rac1-FRET cells were seeded onto the matrices in a 24 well plate at 10^5 cells/mL overnight. Tripods were created from stainless steel grids and autoclaved prior to use in invasion assays. The sterile grid was then placed in a 6 cm dish and media was added, so that the grid was covered. The matrices were then be placed on the grids and an air/liquid interface was formed. This allowed invasion of the cells seeded on top of the matrices as a gradient of cell culture medium was created. A triplicate of matrices per condition was treated daily with vehicle, or the respective Rac1 inhibitors 20 μM EHT 1864 or 50 μM NSC 23766 in DMEM, 10% FBS, 1% P/S and cells allowed to invade for up to 14 days. Following this, the matrices were imaged using the FLIM-FRET analysis outlined below and fixed in 10% neutral buffered formalin (NBF). They were then processed for histological analysis, by paraffin embedding, microtomy and Haematoxylin and Eosin (H&E) as well as automated Cleaved Caspase-3 (CC3) and Ki-67 staining were performed as described below.

Shear Stress and FACS analysis

Shear stress was performed as described previously (Barnes et al., 2012; Vennin et al., 2017). MMTV-PyMT;Rac1-FRET cells were cultured in T75 culture flasks for 72 hours prior to shear stress ± 50 μM NSC 23766 refreshed daily to reach confluence on the day of shear stress. Cells were trypsinized and centrifuged for 5 min at 300 x g. After filtering through 100 μm cell strainers, the cell suspension was diluted to 5 × 10^5 cells/mL in culture medium. Cells in approximately 9 mL of this suspension were then subjected to shear stress while a second aliquot was kept as a passage 0 control (P0). Cells were subjected to five repeated exposures of shear stress (P5) at an automated constant flow rate of 100 μl/sec through a 30-gauge needle. Here, shear stress was measured using Poiseuille's equation; $\tau = 4Q\eta/R3$, with $\tau max = 250$ Pa, Q was the flow rate (0.1 cm^3/s), η was the fluid viscosity of the media (0.78 × 10^{-3} $N.s/m^2$) and R was the radius of the needle (R = 7.95 × 10^{-3} cm). The cells were directly transferred from one needle into the next syringe until all five passages were completed. After recounting the cells, 5 × 10^5 cells per condition (+/− drug and ± shear stress) were seeded in T25 culture flasks for FACS sorting the day after and 1.2 × 10^5 cells seeded on organotypic matrices were used for post-shear stress invasion experiments. Cell death through shear stress ± previous NSC 23766 treatment was assessed by FACS analysis. Briefly, cells were trypsinized and centrifuged as described before and then resuspended in FACS buffer containing 1:500 Annexin V-Cy5 (BioVision) and 1 μg/mL Propidum iodide (PI, Sigma-Aldrich). Mono-stained and unstained cells were used as controls. The culture media from overnight incubation and the PBS from the washing step were collected as well to avoid exclusion of dead floating cells from the analysis. The cells were passed through the 100 μm filter mesh containing lids into FACS tubes to obtain mainly single cells and flow cytometry was performed using FACS Canto II (Becton Dickinson). The acquired data was analyzed using FlowJo software (version 7.6, Tree Star Inc.) and Prism 8 (GraphPad).

Cellular derived matrix (CDM) attachment assay

CDMs were established as described previously (Cukierman et al., 2001). For CDMs constructed on glass, the surface was coated with 2% Gelatine (Sigma, G1393) and allowed to set at 37°C for 2 hours then rinsed twice with Dulbecco's PBS and formalin fixed at room temperature for 30 min. Fixed gelatine crosslinks were quenched in 1 M sterile glycine (Sigma, G7126) for 30 min at room

temperature and coated plates rinsed twice with PBS and once with DMEM prior to cell seeding. TIFs were allowed to expand until confluent. Ascorbic acid (50 mg/ml) was then added to refreshed medium every other day for 7 days. TIFs were removed at day 7 (Extraction Buffer: 0.5% (w/v) Triton X-100, 20 mM Ammonium Hydroxide, 1% (w/v) Sodium Deoxycholate) and CDMs were rinsed with Phosphate buffer saline (PBS) prior to seeding cancer cells and imaging. Cell adhesion was imaged up to 24 h on a live cell microscope (Leica DMI 6000), prior to (P0) and post shear stress (P5) with the differential interference contrast (DIC) Z stacks at 2.5 μm steps for 50 μm acquired every 30 min, with 3 regions of interest (ROIs) imaged per condition per time point. Following acquisition, images were processed in ImageJ (NIH), by Z stack projection, application of a Gaussian Blur at $\sum = 2$ and background subtraction to remove the CDM background, prior to automatic thresholding and area coverage calculation of attached cells. Values were normalized to the t = 0 control reading of each timeseries and presented as fold changes. For FLIM analysis of MMTV-PyMT;Rac1-FRET cell attachment, 10 cells per condition per time point were imaged in an untreated control and cells treated with NSC 23766. The recorded values were then plotted and analyzed in Prism 8 (GraphPad).

Anchorage Independent Growth (AIG) Assay

AIG assays were set up as described previously. Briefly, autoclaved solutions of Low Melting Point Agarose (SeaPlaque Agarose, Lonza) at 10% and 3% (w/v) were melted in a waterbath at 42°C or microwaved shortly and diluted in phenol red free medium (DMEM, 10% FBS, 1% P/S, 5 μg/mL insulin, 10 ng/mL EGF and 10 ng/mL Cholera Toxin A) to reach a final concentration of 1%. A bottom layer of 750 μL 1% Agarose was poured into a 24 well glass bottom dish and left to solidify for 45 min at room temperature. Afterward, molten 3% Agarose was diluted to 0.3% with the appropriate phenol red free medium. The 0.3% Agarose was then mixed at a 2:1 ratio with medium containing the trypsinized, centrifuged and resuspended MMTV-PyMT;Rac1-FRET cells to a final concentration of 10,000 cells per well for a 0.2% Agarose to be obtained. The mixture was added on top of the base layer, so that growth of single cells within this layer could be observed and imaged. After 45 min at room temperature, 1 mL of phenol red free medium was added on top of the Agarose layers. Wells were treated with 50 μM NSC 23766 for 4 h and 24 h respectively and FLIM-FRET imaging performed as described below.

Immunohistochemistry

Tissues and organotypic matrices were fixed in 10% Neutral Buffered Formalin for 24 hours, processed on the Leica Peloris II and embedded in paraffin using the TissuTek Embedding Station. 4 μm sections were cut using Leica Microtome RM2235, sections were placed on Superfrost Plus Slides and allowed to incubate in a 60°C oven for 2 h and overnight for tissues and organotypic matrices, respectively. Slides were deparaffinised with xylene and rehydrated with washes in decreasing concentrations of ethanol, performed on the Leica Autostainer XL. The same autostainer was used for H&E staining and counterstaining with Haematoxylin (Shandon Instant Haematoxylin Kit), before the slides were automatically coverslipped with the Leica CV5030 Robotic Coverslipper and left to dry overnight. The Aperio Scanscope image capture device was used to acquire images of all slides at 20x magnification. Total number of metastasis per lung were quantified per mouse up to 1 mm depth at 100 μm steps in serial sections by examination in QuPath (v0.2.0-m8; Bankhead et al., 2017).

Stainings for Cleaved Caspase-3 and Ki67 were performed as described previously (Vennin et al., 2017, 2019) with a Leica Bond RX fully automated research stainer and the Leica Bond Polymer Refine Detection kit. Heat-induced epitope retrieval with Bond Epitope Retrieval Solution 2 (EDTA based, pH 9) at 93°C for 30 min and 20 min was performed for Ki67 and CC3 staining respectively and at 100°C for 40 minutes for phospho-PAK (S199). The slides were stained according to the IHC-F 60 min Ab incubation protocol using either a 1:500 dilution of the Ki67 Rabbit antibody (ThermoScientific), a 1:200 dilution of the Cleaved Caspase-3 Polyclonal Rabbit antibody (Cell Signaling) or 1:25 for phospho-PAK (S199) (Cell signaling) as primary antibodies (see Figures S1D,E,I and S4A,B and G). Slides were counterstained, coverslipped and scanned as described above. Phospho-PAK (S199) stained section were quantified using QuPath (v0.2.0-m8), with DAB and hematoxylin optical densities computed for each pixel using color deconvolution and border and central regions of tumors manually identified. A watershed cell detection based on the hematoxylin counterstain was used to identify nuclei within these regions. Single cells were identified by applying a 5 μm nuclei detection radius and the average DAB optical density computed for each cell. Using a constant threshold applied, cells were classed as either positive or negative for DAB staining and values averaged for 5 to 6 tumors per condition.

Western Blotting and Rac1 Pulldown

Cell lysates were prepared in RIPA lysis buffer (50 mM HEPES, 1% Trition X-100 (v/v), 0.5% Sodium deoxycholate, 0.1% SDS, 0.5 mM EDTA, 50 mM NaF, 10 mM NA_3VO_4 and 1x protease inhibitor cocktail [CompleteTM Mini, EDTA-free, Roche]). Protein concentration was determined by Bradford (Bio-Rad Protein Assay Dye Reagent Concentrate) assay and volumes adjusted according to measurements. Protein separation was performed by gel electrophoresis using 4%–12% Bis-Tis Protein Gels (NuPageTM, ThermoFisher Scientific), and transferred onto PVDF membranes (Immobilon-P, Millipore) and blocked at room temperature in 5% (TBST) skim milk in TBST. Rinsed (TBST) membranes were incubated overnight at 4°C in primary antibody solutions (TBS/BSA). Primary antibodies were diluted in 1% BSA in TBST at 1:500 for anti-Rac1 (Cytoskeleton), 1:1,000 for anti-GFP (abcam), 1:1,000 for Cyclin-A2 (abcam), 1:1,000 for Cyclin-B1 (Santa Cruz Biotechnology), 1:1,000 for Beta-actin (Sigma), 1:1,000 for phospho-PAK (S199) and at 1:5,000 anti-GAPDH (Cell Signaling). TBST rinsed membranes were then incubated with HRP-linked secondary anti-rabbit and anti-mouse antibody (GE Healthcare, 1:5,000, diluted in 1% skim milk/TBST), for 2 hours at room temperature.

Ultra-ECL and ECL reagents (Western Lighting Plug-ECL, PerkinElmer) were used to visualize signal imaged on a Fusion FX (Vilber). GAPDH was used as a loading control and the levels of endogenous Rac1 in 3 MMTV-PyMT cell lines (isolated from mice without biosensor expression) compared to the MMTV-PyMT;Rac1-FRET cell line.

For the Rac1 pulldown MMTV-PyMT;Rac1-FRET cells were seeded in 10 cm^2 dishes at a density of 8 × 10^6 cells. Dishes were supplemented with serum-free medium overnight and differential amount of wounds performed per dish (zero, single and multiple [60 per 10 cm^2 dish]). Samples were isolated on ice, snap frozen and processed as per the manufacturer's instructions (Cytoskeleton, Rac1 Pull-down Activation Assay) using GST-tagged PAK-PBD protein beads to pull-down GTP loaded Rac.

Mammary imaging window

The application of mammary imaging windows for *in vivo* imaging and their insertion into the skin was described previously (Kedrin et al., 2008; Nobis et al., 2017) and was performed following the standard operation procedure 'Mammary Window Surgery' approved by the Garvan/St Vincents Animal Ethics Committee (ARA 16/13, 19/13). All surgical instruments were autoclaved in Steriilope steam sterilization autoclave bags or by using a bead steriliser (Germinator) and equipment and surfaces were sterilized by wiping down with 70% ethanol. Cyanoacrylate was applied to the edges of a titanium ring (Russel Symes & Company) and a coverslip of 12 mm diameter was placed into the inset of that ring 24 h prior to surgery. The window was disinfected with 70% ethanol end kept in a sterile 50 mL tube after excess glue had been removed and the tightness of the window had been assessed. 24h prior to and at least 72 h post surgery 5 mg/kg of Carprofen (Rimadyl; Ingrao et al., 2013) was administered to the mice in the drinking water.

Anaesthesia was induced and maintained by inhalation of the gas isoflurane using a calibrated vaporizer. The animal was first placed in a chamber containing 4% isoflurane in O_2 and maintained unconscious by ventilation of 1.5%–2% isoflurane in O_2 via a mask using a Bain pediatric circuit. The mouse was then placed on a heating pad to maintain the body temperature and the eyes were lubricated with eye ointment (LacriLube) to prevent dehydration. Anaesthesia with regular reflex testing on the footpad was maintained throughout the entire procedure. Subcutaneous injection of 100 μL of 0.075 mg/kg buprenorphine was used for further pain management prior to and 6h after the surgery. The incision site was shaved to clear any hair, depilated using hair removal cream (Nair) and disinfected using 0.5% chlorhexidine/ 70% ethanol. An incision was made in the skin overlying the palpable tumor using microdissection scissors and the skin blunt dissected around the incision site. A purse string suture was applied through the skin around the incision. The imaging window was then placed into the incision by careful insertion of the skin into the lateral groove of the window. Subcutaneous aspiration of any trapped air beneath the window allowed for a tight fit of the window to the tumor mass. The mice were allowed to recover for 72 h post-surgery and weaned off Carprofen prior to *in vivo* imaging being performed. Recovery gel and/or sunflower seeds are provided to aid recovery post-surgery and in order to minimize damage to the window by the mice and cage surroundings, metal food hoppers and plastic domes are removed from the cages and feed supplied in food trays on the floor of the cage. Paper mache domes with the bottom of the entry hole removed are supplied as cage enrichment along with tissues as nesting material.

In vivo and *Ex vivo* Imaging, Single Cell FLIM analysis and Motion Correction

Excised tumors or lungs were imaged *ex vivo* for a maximum of 30-60 minutes post removal. For lung imaging in the control setting 52 ± 14 cells per mouse and in the NSC 23766 treatment cohort 53 ± 20 cells per mouse were detected and imaged. Mice bearing an optical window were imaged under 1%–2% isoflurane on a heated stage (Digital Pixel, UK) prior to and after i.p. injection of the H_2O vehicle, 4 mg/kg or 8 mg/kg NSC 23766 respectively. For imaging of Rac1 activity away from the vasculature > 175 cells per mouse model were recorded. *In vivo* imaging was performed as described previously on a Nikon Eclipse TE2000-U inverted microscope with an Olympus long working distance 20 × 0.95 NA water immersion lens. A Titanium:Sapphire (Ti:Sapphire) femtosecond pulsed laser (Coherent Chameleon) was used as an excitation source tuned to optimal ECFP excitation wavelengths of 840 nm. A dichroic filter (Chroma 455 nm) was used to separate the second harmonic signal from the donor ECFP. SHG and ECFP signals were passed through band pass filters (Semrock 435/60 and 460/60 respectively) and detected by non-descanned detectors (Hamamatsu). For FLIM a 16-anode PMT (FLIMx16, LaVision Biotec) was used for time correlated single photon counting (TSCPC). Fluorescent lifetimes were analyzed using ImSpectorPro (Version 2.5.0.0, LaVision Biotech) by computing the half-life (τ) of the single exponential function fit to the fluorescence decay data. Lifetime maps were further generated with intensity thresholds set to the average background pixel value for each recording. The raw data was smoothed 3 × 3 and a standard rainbow color look up table (LUT) applied. Finally, for smoothing purposes, a 5 × 5 median filter was further applied. Alternatively, multi-photon imaging was performed using a Leica DMI 6000 SP8 confocal microscope using a 25 × 0.95 NA water immersion objective on an inverted stage. The Ti:Sapphire femtosecond laser (Coherent Chameleon Ultra II, Coherent) excitation source operating at 80 MHz was tuned to a pumping wavelength of 840 nm. RLD-HyD detectors were used with 435/40 nm and 483/40 nm bandpass emission filters to detect the second harmonic generation (SHG) of the collagen I and ECFP respectively. For imaging of the local tumor vasculature non-targeted Quantum dots 655 (Qtracker655) were injected i.v. in the tail vein of mice and imaged using either 840 nm Ti:Saph or an optical parametric oscillator (OPO) tuned to 1120 nm excitation and a 617/60 filter. Images were acquired at a line rate of 700 Hz, 512x512 pixel and at a total of 203 frames per image. Realignment of the data was performed using Galene (v2.0.2; Warren et al., 2018) using the warp realignment mode, 10 realignment points, a smoothing radius of 2px and a realignment threshold of 0.4 applied for the SHG channel and 0.6 for the ECFP signal. Single cell analysis was performed using either ImspectorPro (v2.5.0.0) or FLIMfit (v5.1.1) by drawing ROIs around the cell membranes (see Figures S1C and S3F) and thresholding. For *in vitro* imaging a merged image of

the FLIM signal and the intensity is shown to highlight subcellular structures such as the plasma membrane more clearly, while for the majority of images so purely the FLIM heatmaps are depicted. For the lung imaging a phasor segmentation was performed to remove tissue autofluorescence and isolate the FLIM signal of the Rac1-FRET reporter. For Dendra2 imaging the Ti:Sapphire laser was tuned to excitation wavelength of 920 nm. The green and red fluorescence of the photoconvertible protein and SHG signal from collagen I were detected using 525/50 nm (Chroma), 585/40 nm (Chroma) and 435/40 nm (Semrock), respectively. For photoswitching a 405 laser was used and selected areas of 93.18 μm x 93.18 μm up to 133.21 μm x 133.21 μm in a 465.91 μm x 465.91 μm field of view (FOV) were exposed to a line rate of 400 Hz for up to 30 s. Z stack images were acquired at 2.5 μm steps for up to 150 μm depth. The area of photoswitched cells was quantified in ImageJ (NIH), by Z-projection of the Dendra2-red collected Z stacks and normalization of the area measured to the control photoswitched regions at t = 0. Fold changes in area per region 3-4 regions per mouse per condition were plotted and analyzed using Prism 8 (GraphPad).

QUANTIFICATION AND STATISTICAL ANALYSIS

Statistical analysis was performed using Prism 8 (GraphPad, v8.4.3) software and the following tests performed as indicated in the respective figure legends: unpaired t test with a Welch correction, Kruskal-Wallis test, One-way ANOVA, Sidak Two-way ANOVA and a log-rank Mantel-Cox test for survival. Significances were reported as **** $p < 0.0001$, *** $p < 0.001$, ** $p < 0.01$, * $p < 0.05$.